ICARUS 117, 287–312 (1995)

Simulations of Dense Planetary Rings

III. Self-Gravitating Identical Particles

HEIKKI SALO[1]

Instituto de Astronomia, Universidad Nacional Autónoma de México, Apartado Postal 70-264, Mexico City, DF, Mexico
E-mail: heikki@astroscu.unam.mx

Received April 14, 1994; revised April 21, 1995

The dynamical behavior of collisional ring systems is studied via a local simulation which includes mutual gravitational forces between particles. Direct force calculations involving up to a few thousand identical particles are employed, with parameter values appropriate to Saturn's rings. Different factors affecting the collisional steady state are studied, including two-particle gravitational encounters, the formation of collective Julian–Toomre wakes, and even the development of particle groups.

These simulations indicate that the equilibrium radial velocity dispersion c_x tends to be dominated by that factor which alone would yield the largest random motion. In the case of a constant coefficient of restitution ε among nongravitating particles, the equilibrium c_x never exceeds a few times $r\Omega$, where r is the particle radius and Ω is the orbital angular velocity. With self-gravity, gravitational encounters soon dominate, even when the surface density is small, and c_x is then close to the escape speed from individual particles. With increased surface density, scattering by collective wakes becomes yet more important, and c_x corresponds to the Toomre parameter $Q_T \approx 2$. For Saturn's A-ring this implies a multilayered structure with strongly enhanced velocity dispersion, c_x, reaching values $\approx 15 r\Omega$ for surface densities ≈ 500 kg m^{-2}. The implied $c_x \approx (r/1m)\ 0.2$ cm s^{-1} agrees qualitatively with estimates based on the damping of density waves. Gravitational wakes are also expected for the rings of Uranus.

In principle, velocity-dependent dissipation corresponding to values $\varepsilon \gtrsim 0.6$ would suppress the wake structure. However, the azimuthal asymmetry of Saturn's A-ring gives strong support to the existence of wakes, with the simulated pitch angles of order 20°–25° being in good agreement with those required by observations. This agreement suggests that the effective values of ε in that ring is closer to zero than implied by recent laboratory experiments of impacts between solid ice balls.

Likewise, assuming reasonable densities and dissipation, the present simulations indicate for Saturn's rings that the collective wakes begin to degrade into actual particle groups at distances $a \gtrsim 125{,}000$ km from that planet. Beyond $a \approx 140{,}000$ km, such clumps seem to be very stable. The simulated aggregates have $r_p \approx 0.7$–0.9, where r_p is the minor axis radius of the agregate relative to its Hill's radius.

1. INTRODUCTION

The dynamics of dense particulate rings like the main components of Saturn's rings are dominated by frequent mutual impacts between macroscopic icy particles. Their local equilibrium is determined by the balance between energy loss in inelastic impacts and the viscous gain of energy from the systematic orbital velocity field (see, e.g., Stewart *et al.* 1984). The time scale required to attain such a local equilibrium is very short, corresponding to a few tens of impacts per particle, or less than 10 orbital revolutions in dense rings. In the absence of self-gravity or external perturbations, the local equilibrium is determined mostly by the elastic properties of the particles, more dissipation leading to a smaller velocity dispersion. However, particles of a finite size always retain a residual velocity dispersion that is at least comparable to the difference in orbital motion over one particle diameter. The equilibrium state is also affected by the size distribution, with smaller particles generally exhibiting a somewhat larger velocity dispersion, and by the optical thickness τ, since a reduced mean path between impacts makes the viscous gain of energy less efficient and leads to smaller random motions in regions of larger τ.

The inclusion of mutual gravitational forces affects the local dynamics of collisional systems in several, partially competing ways. For example, in a flattened system with even a moderate surface density the mean vertical gravity can become comparable to or even exceed the corresponding component of the central force. This tends to reduce the geometric thickness quite markedly, both because of the increased vertical stiffness and via increased dissipation due to the enhanced impact frequency (Salo and Lukkari 1982). Their combined effect was simulated by Wisdom and Tremaine (1988, hereafter WT), who used

[1] On leave from: Department of Astronomy, University of Oulu, Finland.

0019-1035/95 $12.00

a constant vertical oscillation frequency 3.6 times larger than the orbital frequency, and by Salo (1991), who calculated the self-consistent vertical field iteratively from the particle distribution; the results were practically identical. However,the inclusion of horizontal components of the self-gravitational field changes the picture more drastically. First, the gravitational encounters between particles correspond to totally elastic impacts and as such they always tend to increase the random velocity dispersion (e.g., Cuzzi *et al.* 1979, Hämeen-Anttila 1984). Second, if the surface density is high enough, there is a possibility of strong collective gravitational effects, analogous to the formation of wakes in stellar systems (Julian and Toomre 1966). Indeed, with the use of standard parameter values for Saturn's rings it can be shown that the B-ring is likewise susceptible to wake formation (Salo 1992b). Third, as the Roche distance is approached, direct accumulation of particles becomes possible, with the wakes transforming to temporary particle groups which resemble the "dynamical ephemeral bodies" (DEBs) proposed by Weidenschilling *et al.* (1984; see also Longaretti 1989). Such signs, too, have been observed in simulations (Salo 1992b).

Most of the existing theoretical studies of gravitating collisional systems have concentrated on the simultaneous effects of impacts and encounters only for systems with low optical thicknesses (e.g., Hornung *et al.* 1985, Stewart and Wetherill 1988, Ohtsuki 1992). The effects of finite particle size have tended to be ignored. Studies of dense systems have typically included only the overall self-gravitational field (e.g., Salo and Lukkari 1982, Araki and Tremaine 1986, Araki 1991). Even when both the mean field and two-particle encounters have been considered (Hämeen-Anttila 1984, Hämeen-Anttila and Salo 1993), no allowance has been made for the collective wakes. On the other hand, such spiral wakes have already been studied extensively in the context of disk galaxies via local simulations (Toomre 1990, Toomre and Kalnajs 1991), though there with much less need for any physical collisions.

The present study, although somewhat idealized to identical particles, attempts to close this gap between collisional and collective effects in the treatment of dense planetary rings. Various factors affecting the equilibrium velocity dispersion are analyzed via local simulations, including mutual impacts, encounters, and the formation of wakes and aggregates. Section 2 describes simulation methods, Section 3 presents preliminary tests, and Sections 4–6 address factors affecting wake formation (surface density, elasticity, radial distance). Section 7 examines particle groupings.

2. SIMULATION METHODS

The simulations of the present study are carried out with a local simulation method that was first applied to planetary ring dynamics by WT and to disk galaxies by Toomre (1990). Just as in those papers, all calculations here are restricted to a small co-moving region within the rings, with periodic boundary conditions as described in detail in WT to take into account the shearing motion. Compared to WT, all self-gravitational forces are now taken into account, rather than just the vertical self-gravity in an approximate manner. Compared to the galactic simulations of Toomre, physical impacts between particles are now included, but any softening of the short-range gravity is omitted as unnecessary.

The calculation of particle orbits is based on integrations of the linearized equations of motion (Hill 1878)

$$\begin{aligned} \ddot{x} - 2\Omega\dot{y} + (\kappa^2 - 4\Omega^2)x &= F_x \\ \ddot{y} + 2\Omega\dot{x} &= F_y \\ \ddot{z} + \Omega_z^2 z &= F_z. \end{aligned} \tag{1}$$

Here the x-axis points in the radial direction, the y-axis points in the direction of orbital motion, and the z-axis is perpendicular to the equatorial plane. The reference point of the coordinate system moves with angular velocity of Ω in a circular orbit at a radial distance a. In the present case of a central point mass, the epicyclic frequency κ and the frequency Ω_z of vertical oscillations are both identical to Ω. As remarked by previous authors, the above linearized equations are valid if $|x|$ and $|z| \ll a$.

The calculation of the gravitational accelerations on the right-hand sides of Eqs. (1) is performed by direct summation: a circular region with radius $R_{\max}$ is chosen around each particle and the forces only from the particles within this region (nearest images, see Fig. 1) are added together. The horizontal force components from the region outside $R_{\max}$ are assumed to vanish due to cancellation. Also, with the simulation parameters of the present study, the net vertical force due to particles outside $R_{\max}$ amounts to only a few percent of the total vertical self-gravity, and it is likewise ignored.

Two different methods are used in the calculations of impacts: (1) the locations of impacts are searched iteratively and the corresponding collisional velocity changes are calculated, (2) particle orbits are integrated through impacts, including mechanical pressure forces arising between slightly overlapping particles. The first method is the same as used by Salo (1992a) in previous simulations of nongravitating dense rings with a broad distribution of sizes, as well as in the brief study by Salo (1992b) of self-gravitating models for Saturn's rings. The latter method, yet to be described in detail, was developed during the course of the present study in order to improve the treatment of particle aggregates.

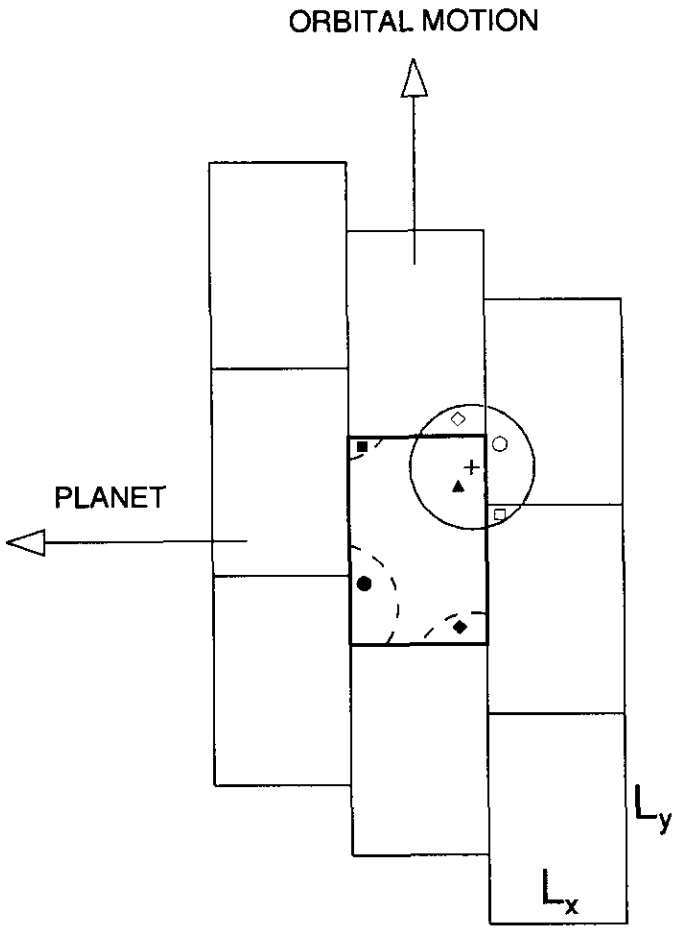

FIG. 1. Schematic diagram displaying the simulation cell (thick lines) and its eight surrounding replicas (thin lines). Gravitational forces on a given target particle (denoted by the cross) are calculated from all the other particles whose nearest image lies within the distance R_{max} (denoted by the large circle). The nearest image can be either the actual particle or one of its eight copies; an example of the former case is given by the filled triangle, while the other filled symbols represent particles having one of their images (open symbols) closer to the target particle. Broken curves indicate regions from which particles contribute to the force felt by the target particle via their images. In the present simulations each particle is included only once, by insisting that $R_{max} \leq \frac{1}{2} \min\{L_x, L_y\}$, where L_x and L_y are the radial and tangential extents of the simulation cell, respectively.

(*a*) *Previous Simulation Method: Search for Impacts*

In the first method particle orbits follow Eqs. (1) between successive impacts and are integrated with an RK4 integrator. In the beginning of each time step a list of potential colliding pairs is constructed, by using a second-order Taylor estimate for the impact locations, which are then iteratively improved to correspond to the fourth-order accuracy (this accuracy is achieved only in the non-gravitating case, as self-gravitational forces are assumed to be constant during the time step). The particle pair with the smallest impact time is chosen and their orbits are followed to the impact time and the collisional velocity changes are calculated (see below). The positions and velocities of the two particles are then extrapolated back to the beginning of the step. All entries in the collision table involving either member of the just-collided pair are recalculated, using their modified positions and velocities. Only impacts taking place after the just-found impact and before the end of the integration step are accepted. After this a new impact with the smallest impact time is chosen and the cycle is repeated until the collision table is empty. The step is finally concluded by integrating all particles to their new locations corresponding to the end of the time step. This method with iterative calculation of several impacts/particle/timestep is very efficient for systems with high impact frequency. For the typical time steps used ($\Delta T = 0.005 \times T_{orb}$, where T_{orb} is the orbital period) radial excursions are of the order of only few tens of centimeters, or less than the typical particle radius. Better accuracy of orbital integrations would have little practical significance in systems with high impact frequency (many particles collide several times during a single dynamical step).

As the gravitational part of the code can be efficiently vectorized (whereas collisional routines cannot), the inclusion of self-gravity does not in itself lead to a large CPU-time increase. Nevertheless, as gravity enhances the impact frequency, the actual computational effort can increase by a large factor, especially if extensive particle grouping occurs. Recently the tree-code method has also been applied to force evaluations in connection with the local method (Richardson 1993): however, with a few thousand particles this does not lead to any substantial increase in efficiency, especially if the impact frequency is high.

The standard impact model for hard spheres is used. The elasticity is described by the coefficient of restitution, ε, determining the amount by which the perpendicular component of the relative velocity component is reduced in each impact. A few experiments with tangential friction have also been performed, in which case particle spins are also taken into account. The velocity change in impact is thus determined by (Salo 1987a)

$$(\mathbf{v}_1)_{coll} = -\varepsilon \mathbf{c}\mathbf{c} \cdot \mathbf{v}_{coll} + (1 - \varepsilon_t)\mathbf{c} \times (\mathbf{v}_{coll} \times \mathbf{c}), \quad (2)$$

where $(\mathbf{v}_1)_{coll}$ and $(\mathbf{v})_{coll}$ stand for the post- and precollisional velocity differences at the contact point, $\mathbf{c}$ for the unit vector joining the particle centers, and ε_t for the coefficient of friction ($\varepsilon_t = 0$ for frictionless impacts). In terms of $\mathbf{v} = \dot{\mathbf{R}}' - \dot{\mathbf{R}}$, the relative velocity of particle centers, $(\mathbf{v})_{coll} = \mathbf{v} - (r\omega + r'\omega') \times \mathbf{c} + (r + r')\Omega\mathbf{N} \times \mathbf{c}$, where r and ω stand for the particle radius and spin-vector (primed and unprimed symbols distinguish the two particles). The last term, $(r + r')\Omega\mathbf{N} \times \mathbf{c}$, where $\mathbf{N}$ stands

for the unit vector in the direction perpendicular to the equatorial plane, arises due to the use of a rotating coordinate system. The changes in the velocity and spin vector of an individual particle follow from the conservation of linear and angular momentum, yielding

$$\dot{\mathbf{R}}_1 - \dot{\mathbf{R}} = \frac{m'}{m+m'}\left\{(1+\varepsilon)\mathbf{cc}\cdot\mathbf{v}_{\rm coll} + \frac{2\varepsilon_t}{7}(\mathbf{v}_{\rm coll} - \mathbf{cc}\cdot\mathbf{v}_{\rm coll})\right\}, \quad (3)$$

$$(r\omega_1 - r\omega) = \frac{m'}{m+m'}\frac{5\varepsilon_t}{7}\mathbf{c}\times v_{\rm coll}, \quad (4)$$

where m and m' are the masses of the impacting bodies. Also, for rotating particles the spin vectors must be transformed to the instantaneous coordinate system before the impact. Most of the simulations study the case ε = constant, but the effects of velocity-dependent elasticity are also addressed, by studying two functional forms for the elasticity (Bridges *et al.* 1984, Dilley 1993). Unless otherwise mentioned $\varepsilon_t = 0$. In order to facilitate the treatment of slow impacts leading to a sliding motion of particle pairs, the same method is adopted as in WT: in all impacts where the perpendicular component of impact velocity falls below $v_{\rm crit} = 0.001r\Omega$, ε is set to unity.

(*b*) *Improved Simulation Method: Force Model for Impacts*

Although the above-described method for the calculation of impacts works adequately for nongravitating particles, as well as for gravitating systems with wake formation, it is not well suited for cases where gravitational sticking between particles leads to the formation of particle aggregates. In this case, overlapping particles become a serious problem. Basically, particle overlaps result from the omission of mechanical pressure forces between impacting particles. Consider two identical, radially aligned, synchronously rotating particles (corresponding to nonrotating particles in the local frame) in contact: the net attraction between them is positive for $a/R_{\rm planet} > (12\rho_{\rm plantet}/\rho)^{1/3}$, where $\rho_{\rm planet}$ and ρ are the internal densities of the central body and the particle, respectively, while $R_{\rm planet}$ stands for the mean radius of the central body (Weidenschilling *et al.* 1984). For icy particles orbiting Saturn this distance becomes about 122,000 km. Thus outside this distance it is expected every now and then that some simulated colliding particle pair with a small velocity difference and a favorable relative orientation have a sufficiently large acceleration toward each other so that after the integration step the particles end up penetrating each other. (Note that overlapping pairs occur also in the case of nongravitating particles, even if the WT method for slow impacts is adopted, because an impact can be occasionally missed because of small inaccuracies in the calculations. This is a less alarming case, however, and the situation is easily corrected at the next step by allowing the overlapping pair to collide at a slightly delayed time. By using double precision in all the calculations, the problem of overlapping particles is totally negligible in the nongravitating simulations.)

Various solutions were attempted to treat sticking particle pairs. For example, setting the mutual acceleration to zero for particles in contact mimics the cancellation of mutual gravity by mechanical pressure. Similarly, in the case of several particles simultaneously in contact, the mechanical pressure forces which are required to balance the net attractions can be solved from a set of linear equations. However, in the case of strong sticking tendencies this was found to be insufficient. Consider what happens when an outside particle hits one of the particles in such a coherently moving group: the velocity impulse causes the target particle to penetrate some other member of the group. Unless some additional pressure force is introduced, the penetrating pair remains overlapping. Also, the artificially enhanced density of the group further increases the tendency for overlaps, easily leading to exaggerated growth of aggregates.

An obvious way out from this problem is to include a model for the actual pressure forces affecting colliding pairs. Such a model is provided by the viscous dissipation model of particle impacts, recently devised by Dilley (1993). In addition to applying this new treatment to aggregates, it turned out to be advantageous to handle all impacts in a similar fashion, and replace the search of impact locations with an additional force term in the right-hand side of Eqs. (1). Somewhat suprisingly, this new method of collisional calculation turned out not only to be capable of treating dense particle aggregates, but also to be faster in general, despite the much smaller time steps required (meaning that during each step, particle motions are typically just a tiny fraction of particle radii). Due to the small step size a simple second-order Taylor integration is utilized.

Dilley (1993) developed his viscous dissipation model to offer a theoretical parameterization for the Hatzes *et al.* (1988) measurements of velocity and size-dependent elasticity in impacts between ice particles. In this model the pressure force between a particle pair is assumed to be composed of a restoring harmonic force and a viscous damping force,

$$F(\alpha) = k\alpha + \beta\dot{\alpha} \quad (\alpha > 0) \\ = 0 \quad (\alpha \le 0), \quad (5)$$

where $\alpha = (r + r') - |\mathbf{R} - \mathbf{R}'|$ is the penetration depth.

The force acts in the direction joining the particle centers: the relative acceleration is determined by $F(\alpha) = -\overline{M}\ddot{\alpha}$, where $\overline{M} = mm'/(m + m')$ is the reduced mass of the pair. Conservation of linear momentum determines individual accelerations:

$$\Delta\ddot{\mathbf{R}} = \frac{m'}{m + m'} F(\alpha)/\overline{M} \frac{\mathbf{R} - \mathbf{R}'}{|\mathbf{R} - \mathbf{R}'|},$$
$$\Delta\ddot{\mathbf{R}}' = -\frac{m}{m'} \Delta\ddot{\mathbf{R}}. \tag{6}$$

The attractive feature of Dilley's model is that the parameters $k/\overline{M}$ and $\beta/\overline{M}$ can be tied to simple physical parameters, namely the duration of the impact and the coefficient of restitution. For an impact between two particles in free space, the equation $F(\alpha) = -\overline{M}\ddot{\alpha}$ has a solution of an exponentially damped oscillation (impact starts at $t = 0$ when $\alpha = 0$),

$$\alpha = \frac{\dot{\alpha}(0)}{\omega} e^{-t/2s} \sin(\omega t), \tag{7}$$

where the modified frequency and damping are characterized by

$$\omega = \sqrt{\omega_0^2 - 1/(2s)^2},$$
$$s = \overline{M}/\beta, \tag{8}$$

where $\omega_0 = \sqrt{k/\overline{M}}$ would be the undamped frequency. The duration of the impact (the length of the first half-cycle) and the coefficient of restitution are (Dilley 1993)

$$T_{\text{dur}} = \pi/\omega \approx \pi/\omega_0$$
$$\varepsilon = -\frac{\dot{\alpha}(T_{\text{dur}})}{\dot{\alpha}(0)} = e^{-\pi/2\omega s}. \tag{9}$$

Thus specifying the desired ε determines the product $(k/\overline{M})^{1/2}(\overline{M}/\beta) = \sqrt{(\omega s)^2 + 0.25}$, while $(k/\overline{M})$ relates to the duration of the impact.

In the present simulations with this method, we have set $T_{\text{dur}} = 0.0025 T_{\text{orb}}$, and employ time steps of $0.0001 T_{\text{orb}}$. As with the previous collisional method, the time interval for calculation of gravitational forces is $0.0050 T_{\text{orb}}$. In practice, a list of close pairs is constructed while gravitational forces are calculated, and the possible penetration is checked only for these nearby pairs. Maximum penetration stays below 5% of the particle radius (the force between a pair of particles is limited to that between particles in exact contact). Detailed comparisons indicate good agreement with the previous collisional calculation method in all experiments with no aggregate formation.

3. PRELIMINARY EXPERIMENTS AND TESTS

In this section the requirements for numerical simulations of gravitating systems are analyzed, and the effects of such simulation parameters as the size of the simulation region or the number of particles are tested. This is very important due to the large computational effort in the experiments including mutual forces between particles. All tests are performed for parameter values which lead to the formation of wakes but not to excessive aggregates.

To demonstrate the qualitative effects of self-gravity, a short preliminary series of simulations was carried out comparing various approximations for the inclusion of mutual forces. The system consisted of $N = 1000$ identical spherical particles, each with internal density $\rho = 900$ kg m^{-3} and radius $r = 1$ m. The width of the square-shaped simulation region was $L = 65$ m and the saturnocentric distance was $a = 100{,}000$ km. This yields an optical thickness $\tau \approx 0.75$ and a surface density $\Sigma \approx 900$ kg m^{-2}. The coefficient of restitution was set to the constant value $\varepsilon = 0.5$. The results of the experiments are seen in Figs. 2 and 3, which compare the cases where self-gravity is either (a) altogether ignored, (b) calculated with the WT method, (c) obtained by the iterative self-consistent method of vertical force calculation (Salo 1991), or (d) by taking into account all mutual force components. In addition, both methods for collisional calculations are compared here.

Among other things, Fig. 2 confirms that the inclusion of vertical force (dashed curves) leads to a strongly reduced geometric thickness as compared to the nongravitating case (thick solid curves). Although the velocity dispersion is less affected, this extra vertical force tends to increase the ratio c_z/c_x of the vertical to radial velocity dispersion. Also evident is that fairly similar results are obtained whether the vertical field is calculated by WT or by the self-consistent method, in agreement with Salo (1991). However, inclusion of the equatorial components of self-gravity (thin solid lines) changes the situation drastically: velocity dispersion increases and it also shows strong fluctuations. Another large change is in the impact frequency: in the nongravitating case it is about 15 impacts/particle/orbital revolution, but with the vertical field it increases to 200–300, and with the inclusion of all force components to about 500. Comparison between the two collisional method (curves with and without symbols) shows excellent agreement in the nongravitating case, as well as in the case of gravitating particles if statistical fluctuations are taken into account. However, with the new method a considerably smaller impact frequency, about 100 impacts/particle/orbit, is obtained. This difference follows from the fact that, whereas in the old method sliding particle pairs experienced numerous small jumps, each sliding impact is counted just once with the newer method.

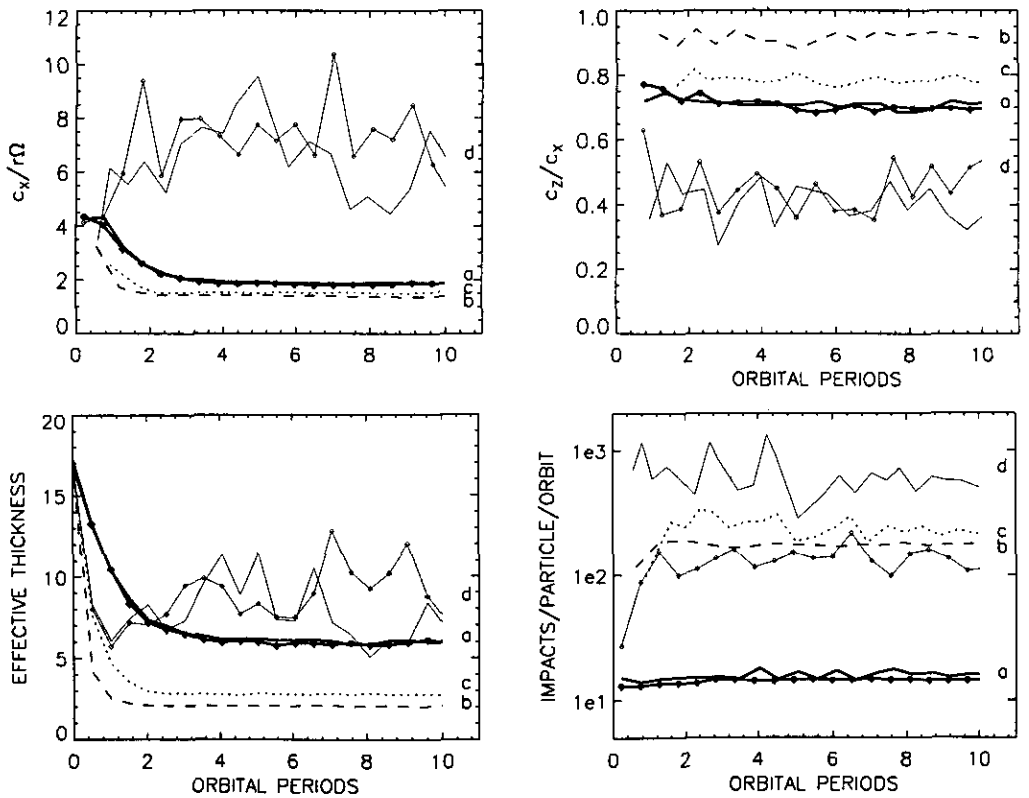

FIG. 2. Comparison between various approximations made in calculating the ring self-gravity. The evolutions of the radial velocity dispersion c_x, the ratio c_z/c_x between vertical and radial velocity dispersions, the effective geometric thickness H, and the impact frequency are all displayed as functions of orbital revolutions. The effective thickness is defined by $H = \sqrt{12\langle z^2\rangle}$, which is the thickness of a homegeneous slab of particles which would have the same dispersion as the observed near Gaussian distribution. Simulation parameters are given in the text. Thick solid lines (a) correspond to nongravitating particles, and thin solid lines (d) to a simulation where all forces are included. Dashed lines (b) denote simulation with the WT method, using a 3.6-times-enhanced vertical frequency, and dotted lines (c) mark the case where self-consistent vertical gravity is included. Solid lines with symbols stand for the new collisional method where impacts are described by elastic forces affecting partially penetrating particles.

Figure 3 shows the particle positions at the end of the simulations of Fig. 2. Comparing the cases without self-gravity and with the vertical field only (using just the WT method, iterative self-consistent field having yielded a practically identical result), one can see the reduction of the vertical thickness as well as traces of the regular structure that would form in the WT-type simulations for somewhat larger τ's. On the other hand, the true self-gravitational case is dominated by collective wake-like structures, forming immediately within the first orbital period, much as Julian and Toomre (1966) and Toomre (1990) had implied. These wakes have a transient structure, constantly forming and dissolving on timescales of somewhat less than an orbital period. The strong fluctuations in velocity are related to these strong instantaneous wakes.

From Fig. 3 it is clear that in order to obtain reliable results in self-gravitational experiments, the size of the simulation region must be considerably larger than the typical scale of the collective wakes. Otherwise, our periodic boundary conditions are likely to distort the scales and pitch angles of the wakes and probably also other quantities like velocity dispersion. The scale of wakes can be roughly estimated from the critical wavelength λ_{cr} related to axisymmetric Jeans instabilities (Toomre 1964) in an infinitesimally thin disk,

$$\lambda_{cr} = 4\pi^2 G\Sigma/\kappa^2, \tag{10}$$

where the epicyclic frequency κ equals Ω in a Keplerian velocity field, and G stands for the gravitational constant. As implied by Julian and Toomre (1966), this near-instability or strong amplification in the shearing disk manifests itself in the form of trailing wavelets whose most prominent azimuthal wavelength is $\approx 2\lambda_{cr}$ for a flat rotation curves, and $\approx 4\lambda_{cr}$ for the present case of a Keplerian velocity field. The axisymmetric instability itself is suppressed at all wavelengths if the radial velocity dispersion exceeds the critical value

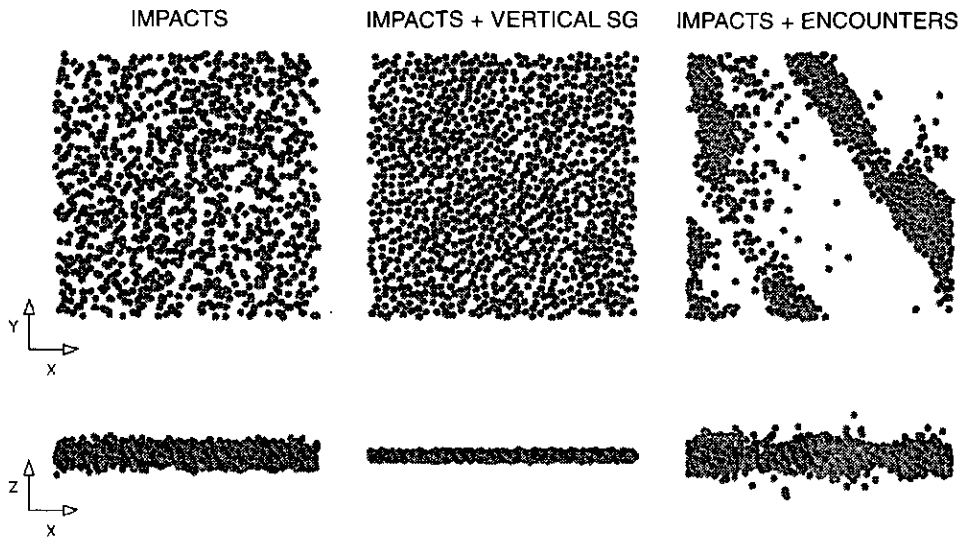

FIG. 3. Particle positions at the end of the simulations of Fig. 2, seen both from above (x, y) and in the direction of the orbital motion (x, z). On the left, self-gravity is not taken into account, in the middle vertical forces are included (via the WT method), and on the right all forces are included. The size of the simulation region is 65 m, and the particles are 1 m in radius.

$$c_{cr} = 3.36G\Sigma/\kappa. \tag{11}$$

However, even for values of the Toomre parameter $Q_T = c_x/c_{cr}$ around 2 the system can retain a significant tendency for the formation of collective trailing wakes (Julian and Toomre 1966).

We next want to formulate the requirements for the size of the calculation region in terms of the number of simulation particles and other physical parameters of the system. For identical particles the surface density is related to optical depth by $\Sigma = \frac{4}{3}\tau\rho r$, and by replacing $\Omega^2 = GM/a^3$, where M is the mass of the central body, we obtain for Saturn's rings ($M = 5.685 \times 10^{26}$ kg)

$$\begin{aligned}\lambda_{cr} &= 69.4\text{ m}\left(\frac{a}{10^8\text{ m}}\right)^3\left(\frac{\Sigma}{1000\text{ kg m}^{-2}}\right)\\ &= 83.3\text{ m}\left(\frac{a}{10^8\text{ m}}\right)^3\left(\frac{\rho}{900\text{ kg m}^{-3}}\right)\left(\frac{r}{1\text{ m}}\right)\tau.\end{aligned} \tag{12}$$

In a simulation system with width L, optical thickness $\tau = N\pi r^2/L^2$, so that

$$\begin{aligned}\frac{\lambda_{cr}}{L} &= 36\,N^{-0.5}\left(\frac{\Sigma}{1000\text{ k gm}^{-2}}\right)^{1.5}\left(\frac{a}{10^8\text{ m}}\right)^3\\ &\quad\times\left(\frac{\rho}{900\text{ kg m}^{-3}}\right)^{-0.5}\left(\frac{r}{1\text{ m}}\right)^{-1.5}\\ &= 47\,N^{-0.5}\tau^{1.5}\left(\frac{a}{10^8\text{ m}}\right)^3\left(\frac{\rho}{900\text{ kg m}^{-3}}\right).\end{aligned} \tag{13}$$

In terms of the total number of particles per cell,

$$\begin{aligned}N &= 1280\left(\frac{\Sigma}{1000\text{ kg m}^{-2}}\right)^3\left(\frac{a}{10^8\text{ m}}\right)^6\left(\frac{\rho}{900\text{ kg m}^{-2}}\right)^{-1}\\ &\quad\times\left(\frac{r}{1\text{ m}}\right)^{-3}\left(\frac{L}{\lambda_{cr}}\right)^2\\ &= 2210\,\tau^3\left(\frac{a}{10^8\text{ m}}\right)^6\left(\frac{\rho}{900\text{ kg m}^{-3}}\right)^2\left(\frac{L}{\lambda_{cr}}\right)^2.\end{aligned} \tag{14}$$

In the case of a nonsquare simulation region, L^2 needs to be replaced by L_xL_y, where L_x and L_y stand for the radial and azimuthal widths, respectively. With realistic Saturn's ring parameters as in Fig. 3, several tens of thousands of particles would be required for $\lambda_{cr} \gg L_x, L_y$ (Fig. 4). In fact in the above simulations with $N = 1000$, the critical wavelength was 62 m, or only about the same as the width of the simulation region. As emphasized by Fig. 4, simulations become very cumbersome when large values of τ are desired. Note that consumption of CPU time scales roughly as N^2, so that in fact CPU time is proportional to $\tau^6(L/\lambda_{cr})^4$. Therefore, to keep CPU time consumption tolerable it is important to estimate the smallest acceptable L/λ_{cr} value still capable of giving results that are approximately correct.

A series of test runs was carried out to check this important question of the adequate size of the simulation region. In Toomre's (1990) noncollisional simulations, calculation cells with $L_x \times L_y = 6\lambda_{cr} \times 8\lambda_{cr}$ were typically used with 4800 particles (whereas in Toomre and Kalnajs 1991 even 12-fold larger particle numbers were simulated). We use here the same surface number density, $n = k/\lambda_{cr}^2$ with $k = 100$. As the collisional simulations operate

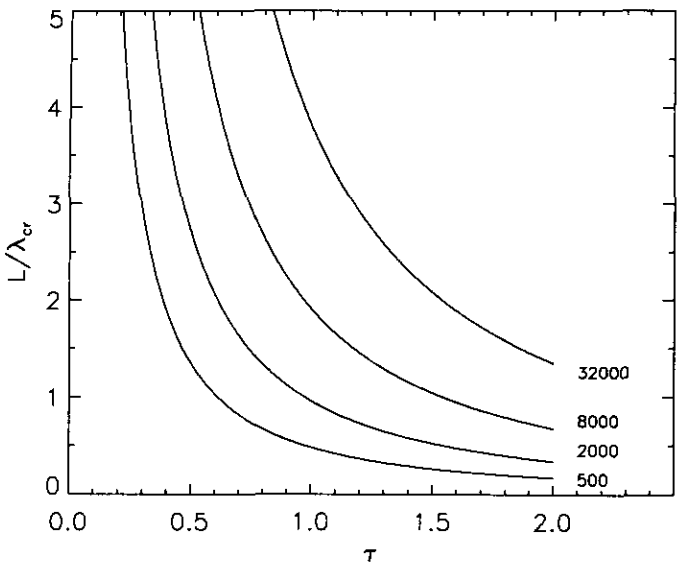

FIG. 4. Size of the simulation region in units of the critical wavelength, shown as a function of optical thickness τ and number of simulation particles. Saturnocentric distance a = 100,000 km and internal density ρ = 900 kg m^{-3} are assumed.

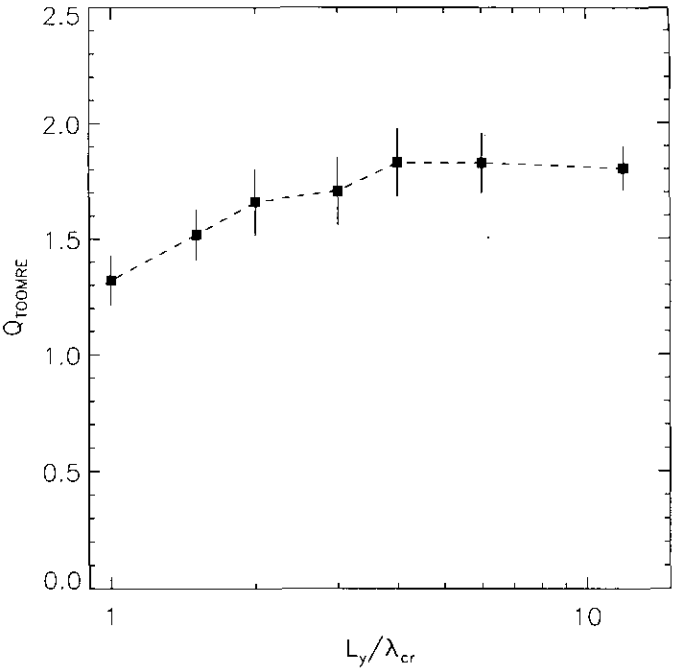

FIG. 5. Influence of the tangential width L_y of the simulation region upon the velocity dispersion, measured via the Toomre parameter $Q_T = c_x/c_{cr}$. In each experiment $L_x/\lambda_{cr} = 4$, and $R_{max} = 1.25\lambda_{cr}$ (or $0.5 \times L_y$, whichever is smaller; see Table I). Asterisks denote two additional simulations, with $R_{max} = 2.0$ and $0.5\lambda_{cr}$ (upper and lower symbol, respectively). Each simulation lasted 20 orbital revolutions and the length of the error bars corresponds to 2 standard deviations during the last 10 orbital revolutions. In each case the number density was 100 particles per λ_{cr}^2.

with finite-sized particles, the number density must be converted to physical quantities. From Eqs. (12) we obtain

$$r = 2.34\ \mathrm{m} \left(\frac{\Sigma}{1000\ \mathrm{kg\ m^{-2}}}\right) \left(\frac{a}{10^8\ \mathrm{m}}\right)^2 \times \left(\frac{\rho}{900\ \mathrm{kg\ m^{-3}}}\right)^{-1/3} \left(\frac{k}{100}\right)^{-1/3}, \quad (15)$$

$$\tau = 0.357 \left(\frac{a}{10^8\ \mathrm{m}}\right)^{-2} \left(\frac{\rho}{900\ \mathrm{kg\ m^{-3}}}\right)^{-2/3} \left(\frac{k}{100}\right)^{1/3}.$$

The same standard parameters for ρ, Σ, and a are assumed as in Fig. 2, so that r = 2.34 m and τ = 0.357. The critical wavelength is 69.4 m. Figure 5 compares the radial velocity dispersion obtained in simulations performed with various sized calculation areas. As the radial extent L_x has less significance (Toomre 1994, personal communication), in most experiments it was fixed to $L_x = 4\lambda_{cr}$, while L_y/λ_{cr} was varied between 1 and 12 (meaning that the total number of particles N = 400–4800). In most cases, $R_{max} = 1.25\lambda_{cr}$. Simulation parameters and observed Q_T values are also collected in Table I.

According to Fig. 5 (see also Table I), the eventual Q_T values are reduced by about 5% for $L_y = 3\lambda_{cr}$ as compared to the value $Q_T = 1.8$ obtained for $L_y = 12\lambda_{cr}$, and by about 15% for $L_y = 1.5\lambda_{cr}$. Even for the smallest tested cell size ($L_x \times L_y = 1\lambda_{cr} \times 1\lambda_{cr}$, with $R_{max} = 0.5\lambda_{cr}$) the

TABLE I
Velocity Dispersions in Experiments with Various Sized Calculation Areas

N	L_x/λ_{cr}	L_y/λ_{cr}	R_{max}/λ_{cr}	Q_T
		L_y (tangential width) varied		
4800	4	12	1.25	1.80 ± 0.09
2400	4	6	1.25	1.83 ± 0.13
1600	4	4	1.25	1.83 ± 0.15
1200	4	3	1.25	1.71 ± 0.15
800	4	2	1.00	1.66 ± 0.15
600	4	1.5	0.75	1.52 ± 0.11
400	4	1	0.50	1.32 ± 0.11
		L_x (radial width) varied		
2400	6	4	1.25	1.84 ± 0.11
1600	4	4	1.25	1.83 ± 0.15
1200	3	4	1.25	1.82 ± 0.18
		R_{max} (gravity cutoff distance) varied		
2400	4	6	2.00	1.97 ± 0.16
2400	4	6	1.25	1.83 ± 0.13
2400	4	6	0.50	1.50 ± 0.06

TABLE II
Size of Calculation Region and the Average Radial Velocity Dispersions in Experiments with Various Internal Densities ρ and Optical Thicknesses τ

ρ (kg m^{-3})	L/λ_{cr}			$c_x/r\Omega$		
	$\tau = 0.1$	$\tau = 0.25$	$\tau = 0.39$	$\tau = 0.1$	$\tau = 0.25$	$\tau = 0.39$
0	—	—	—	2.89 ± 0.06	2.70 ± 0.03	2.38 ± 0.04
255	86.4	21.9	11.1	2.64 ± 0.06	2.41 ± 0.07	2.15 ± 0.05
450	43.2	10.9	5.5	2.73 ± 0.06	2.60 ± 0.05	2.34 ± 0.07
675	28.2	7.3	3.7	2.98 ± 0.07	3.03 ± 0.20	3.08 ± 0.22
900	21.6	5.5	2.8	3.46 ± 0.08	3.83 ± 0.15	5.05 ± 0.41
1125		4.4	2.2		4.73 ± 0.43	6.71 ± 0.81
1350	14.4	3.6	1.9	4.27 ± 0.10	5.96 ± 0.45	9.60 ± 1.8
1800	10.8	2.7	1.4	5.50 ± 0.12	8.01 ± 0.7	11.9 ± 2.4
2250	8.6	2.2		6.39 ± 0.26	12.2 ± 1.2	
2700	7.2	1.8		>15	>30	

Note. The gravity cutoff distance $R_{max} = 0.5L$. Other parameters are: a = 100,000 km, $\varepsilon = 0.5$. In the two simulations leading to stable aggregates, the velocity dispersion of the nonaccreted particles did not attain a steady state.

reduction is only about 30%. Experiments with different R_{max} indicate that the value $1.25\lambda_{cr}$ used in most experiments of Fig. 5 is in fact too small: for $R_{max} = 2.0\lambda_{cr}$, Q_T increases by about 10%, to about $Q_T = 2$. Finally, the comparison between $L_x/\lambda_{cr} = 6$ and 3 confirms that L_x has less influence.

According to these experiments, simulation cells with $L/\lambda_{cr} \geq 4$ should be used, with $R_{max} \geq 2\lambda_{cr}$, in order to obtain results at least for the eventual Q_T's which are accurate to within a few percent. Also, simulations must have long enough durations (>10 orbital periods) so that mean values can be extracted with reasonable confidence despite the large statistical fluctuations. However, in several cases (for large τ or ρ, or for large distances) this requirement would mean excessive CPU time consumption (see Fig. 4; for other ρ and a the required particle number scales proportional to $a^6\rho^2$). Therefore, the goal in the present simulations has been much more modest; in most of the present simulations $L >$ only $2\lambda_{cr}$, and R_{max} = only $0.5L$. This should still lead to about 15% accuracy in velocity dispersion. All values of the simulation parameters used in the experiments that follow are displayed in Tables II–V, so that any reduction in c_x can at least be estimated.

In addition to estimating this modest accuracy of the velocity dispersion, the properties of the wake structures were compared between simulations with various cell sizes. Figure 6 shows examples of the wake structures obtained at the end of several of the above simulations. As can be seen, the obtained structures are qualitatively fairly similar for the two largest cell sizes studied. However, as the calculation region is reduced the artificial regularities imposed by the periodic boundary conditions become more and more severe, affecting both the pitch angle and the scale of the wakes, as we had feared.

For more quantitative estimates, an autocorrelation

TABLE III
Experiments with Various Values of Optical Thickness τ

τ	N	L/λ_{cr}	$c_x/r\Omega$	c_x/c_{esc}	Q_T	f/τ
0.1	400	13.5	3.37 ± 0.13	0.93	4.78	39
0.2	800	6.7	3.55 ± 0.13	0.98	3.55	51
0.3	1200	4.5	4.03 ± 0.22	1.11	1.90	75
0.4	1600	3.4	4.94 ± 0.45	1.35	1.75	108
0.5	2000	2.7	6.65 ± 0.87	1.82	1.88	155
0.6	2400	2.2	9.58 ± 2.33	2.54	2.18	210

Note. The gravity cutoff distance $R_{max} = 0.5L$. Other parameters are: a = 100,000 km, ρ = 900 kg m^{-3}, $\varepsilon = 0.5$. The symbol f stands for impact frequency/particle/orbit. In the nongravitating case $f \approx 6\pi\tau$.

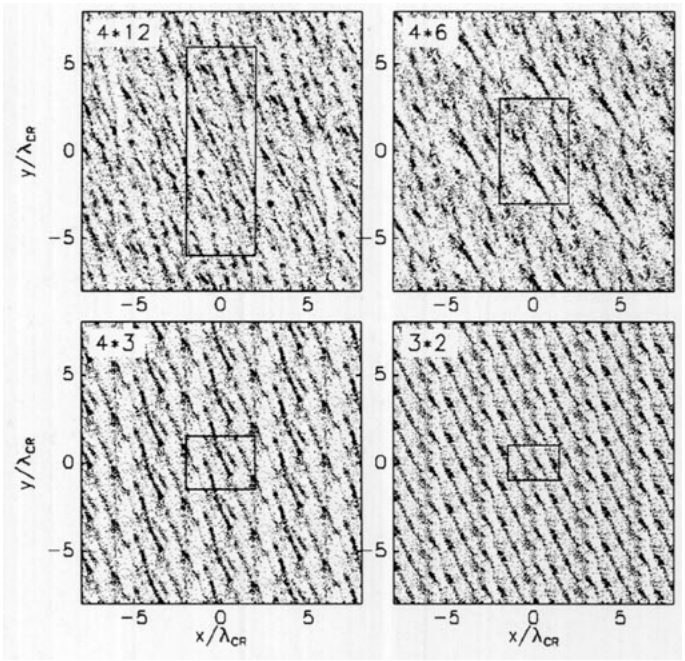

FIG. 6. Examples of variously sized calculations (numbers in frames denote the cell dimensions $L_x \times L_y$), displayed at the end of the simulations. Solid boxes mark the actual calculation cell. Compare to several figures in Toomre (1990), noting that here the orbital motion is up and the direction to the central body is to the left.

analysis was also performed. As we remarked, Toomre and Kalnajs have already carried out very extensive and sophisticated studies of the behavior of collective wakes in two-dimensional systems of noncolliding particles. Especially in Toomre and Kalnajs (1991), they studied the spatial correlation functions between the particle positions and guiding centers. Their numerical simulations showed extremely good agreement with their theoretical predictions based on superpositions of Julian–Toomre-type collective wakes situated around each particle. Their calculation of correlation functions was performed with the help of Fourier transforms of particle and guiding center densities after each timestep.

Figure 7 displays some similar but coarser 2-dimensional autocorrelation functions for the particle positions

TABLE IV
Experiments with Various Values of Constant Coefficient of Restitution ε

ε	Nongravitating $c_x/r\Omega$	Gravitating $c_x/r\Omega$	Gravitating Q_T	Gravitating f/τ
0.1	1.17 ± 0.02	7.2 ± 1.1	2.6	266
0.2	1.29 ± 0.04	7.0 ± 1.2	2.5	
0.3	1.52 ± 0.04	6.3 ± 1.1	2.2	203
0.4	1.82 ± 0.04	5.7 ± 0.7	2.0	
0.5	2.38 ± 0.06	5.0 ± 0.7	1.8	108
0.6	3.65 ± 0.09	4.3 ± 0.3	1.5	
0.65	5.04 ± 0.16	4.4 ± 0.2	1.5	
0.7	Increasing	5.9 ± 1.2	2.1	

Note. In each experiment $N = 1000$ particles were simulated and $L/\lambda_{cr} = 2.56$, $R_{max} = 0.5L = 1.28\lambda_{cr}$. Other parameters are: $a = 100{,}000$ km, $\rho = 900$ kg m^{-3}, and $\tau = 0.4$.

TABLE V
Experiments for Various Distances

a (10^3 km)	L/λ_{cr}	$c_x/r\Omega$	c_x/c_{esc}	Q_T
70	9.8	2.16 ± 0.05	1.00	2.23
80	6.6	2.38 ± 0.08	0.90	1.64
90	4.6	3.09 ± 0.18	0.99	1.50
100	3.4	5.14 ± 0.49	1.41	1.82
110	2.5	8.15 ± 1.23	1.93	2.17
120	1.9	12.0 ± 2.6	2.49	2.45
130	1.5	13.8 ± 2.5	2.56	2.23
135	1.4	15.4 ± 2.6	2.68	2.20

Note. In each experiment $N = 1600$ particles were simulated, $L = 112.1$ m, $R_{max} = 0.5L$. Other parameters are: $\tau = 0.4$, $\rho = 900$ kg m^{-3}, and $\varepsilon = 0.5$.

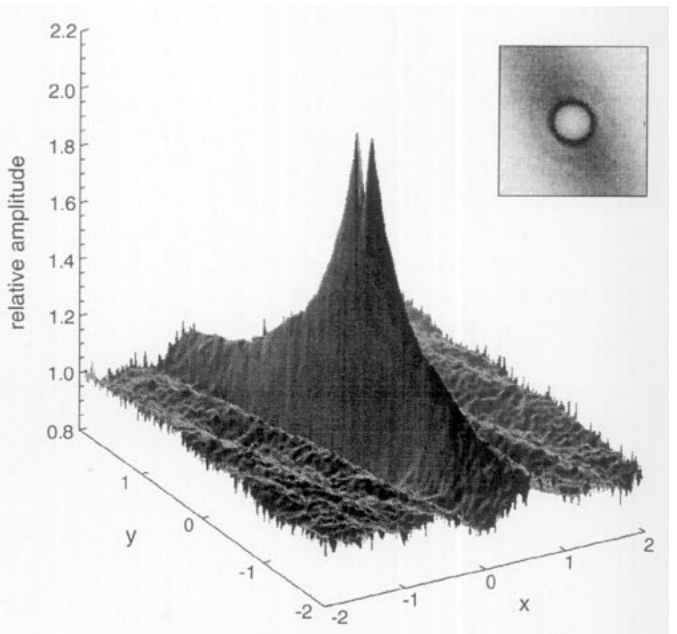

FIG. 7. Two-dimensional autocorrelation function from the simulation with $L_x \times L_y = 4\lambda_{cr} \times 12\lambda_{cr}$. Each particle in turn has been placed at the center and the relative positions of all the other particles have been tabulated, projected onto the equatorial plane. The plots show densities (normalized to the mean density) obtained by adding together positions after each orbital period for $T_{orb} = 10$–20. The dimensions of the plot are $2\lambda_{cr} \times 2\lambda_{cr}$. Compare this with Fig. 9 ($\kappa/\Omega = 1$) in Julian and Toomre (1966). The small insert shows the central peak ($0.25\lambda_{cr} \times 0.25\lambda_{cr}$) region: the two concentric rings there correspond to distances $2r$ and $4r$.

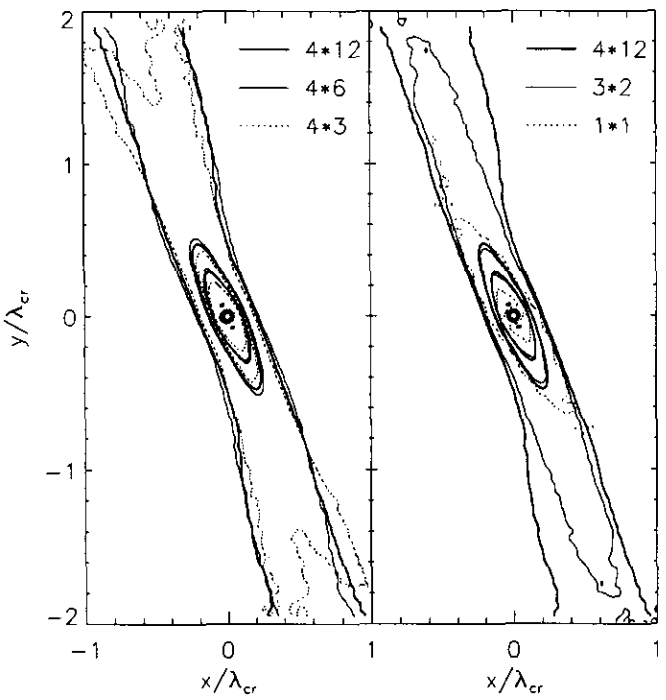

FIG. 8. Comparison of the autocorrelation functions in simulations with different-sized calculation regions. Only the central ridge is displayed; weak negative sidethroughs are omitted. Contours correspond to positive densities of 1.1, 1.4, 1.7, and 2.0 times the ambient.

in the present experiment with $L_x \times L_y = 4\lambda_{cr} \times 12\lambda_{cr}$, projected to the equatorial plane for a region corresponding to $2\lambda_{cr} \times 2\lambda_{cr}$. As the Fourier transforms were not collected during the present simulations, only the individual particle positions (stored once/orbital revolution) were used here, and the autocorrelation function was calculated directly by taking each particle in turn as a reference point and superposing the relative locations of all other particles. Although much more time-consuming than the Fourier technique, it yields better resolution in our case of relatively few particles. For example, the concentric enhancements near the origin in Fig. 7, at distances of $2r$, follow from the particles being temporarely in contact (even another fainter feature is visible at $4r$, indicating a tendency for the formation of small transient groups). The comparison between different-sized simulation regions (Fig. 8) indicates that at least the central portions of the wakes remain fairly similar in all experiments with L_x, $L_y > 2$ or $3\lambda_{cr}$. On the other hand, for the experiment with $L_x = L_y = \lambda_{cr}$, the pitch angle is considerably larger ($\approx 31°$) than for more amply sized calculation cells ($\approx 23°$; the values refer to the innermost dense region within $0.5\lambda_{cr}$) and other features there may be just about as untrustworthy. This artificial dependence of the obtained pitch angle upon the size of the simulation region must be taken into account when the photometric properties of these dynamical models are to be compared with actual observations of the azimuthal asymmetry in the A-ring of Saturn.

4. FACTORS AFFECTING VELOCITY DISPERSION

In the self-gravitating experiments of the previous section, the systems attained a rough steady state with a dimensionless radial velocity dispersion $Q_T \approx 2$, with this steady state arising from a balance between collisional cooling and the scattering by the shearing wakes constantly forming and reforming due to collective amplification of the N-body graininess. However, with a wider range of physical parameter values at least two other factors are likely to affect the equilibrium, namely the minimum velocity dispersion due to collisions between finite sized particles, and the gravitational scattering from two-particle encounters. For example, if the surface density is very low, collisions in a differentially rotating disk are likely to maintain a minimum velocity dispersion that exceeds c_{cr} by a such a large factor that any collective wakes are at best very feeble. Also, once very massive particles are included, their mutual gravitational encounters may keep the system so hot that collective phenomena are again strongly suppressed. In the following we write simple estimates for the various parameter domains where all three factors are likely to dominate, and compare these estimates with our simulations.

According to several previous simulation studies, as we remarked in the Introduction, impacts can always maintain a certain minimum velocity dispersion proportional to the orbital velocity difference

$$\frac{c_{imp}}{r\Omega} \approx 2\text{–}3, \tag{16}$$

over one particle diameter, for all τ's. This lower limit corresponds to a near-monolayer ring resulting from $\varepsilon =$ constant, though in realistic cases with $\varepsilon = \varepsilon(v)$ decreasing with increasing v, a somewhat higher velocity dispersion can be achieved (see Section 5). On the other hand, dilute gravitational encounters will always tend to produce relative velocities on the order of the escape speed from the particle surface, $v_{esc} = \sqrt{2Gm/r}$, where m is the mass of each separate particle. Expressed in terms of $r\Omega$ this yields the minimum

$$\frac{c_{enc}}{r\Omega} = 3.64 \left(\frac{a}{10^8\ \mathrm{m}}\right)^{1.5} \left(\frac{\rho}{900\ \mathrm{kg\ m^{-3}}}\right)^{0.5}. \tag{17}$$

Finally, from Eq. (11), inserting Saturn's parameters and assuming $Q_T = 2$, the velocity dispersion due to wakes can be expressed as

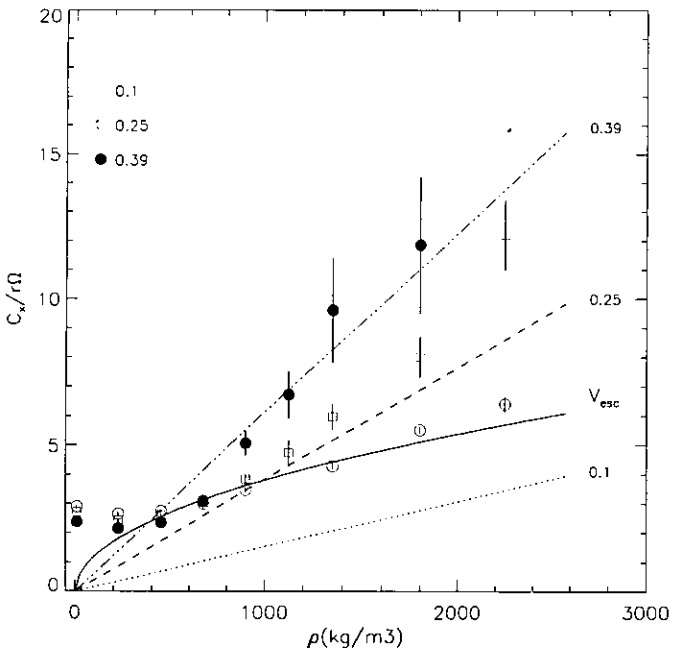

FIG. 9a. Radial velocity dispersion in units of $r\Omega$ as a function of particle internal density ρ, for $\tau = 0.1$, 0.25, and 0.39. The distance is fixed to $a = 100{,}000$ km and $\varepsilon = 0.5$. The solid curve denotes the escape velocity from particle surfaces (c_{enc}), while various dashed lines denote the $Q_T = 2$ dependence (c_{wake}) for the different τ values. Symbols stand for the observed steady-state values in simulations, with error bars indicating their dispersion.

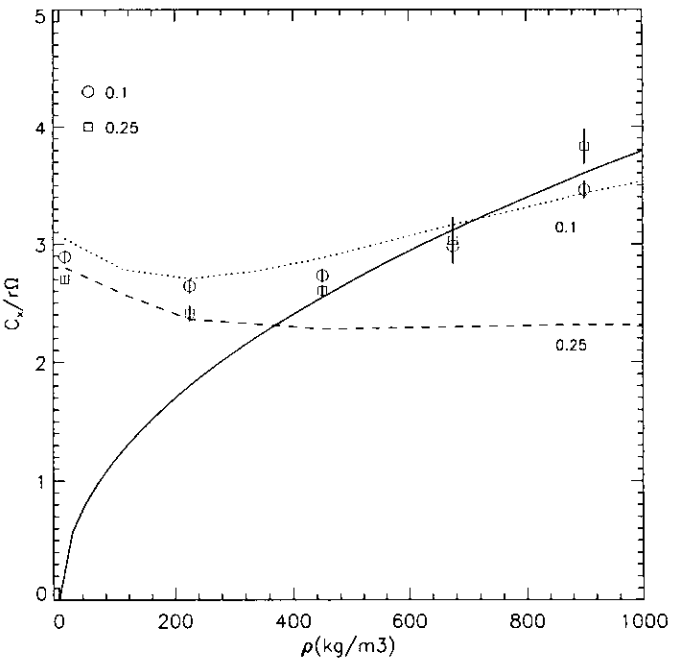

FIG. 9b. Detail, showing the theoretical curve for the combined effects of collisions and encounters without inclusion of collective wakes (calculated according to Hämeen-Anttila and Salo 1993). For clarity, only curves for $\tau = 0.1$ and 0.25 are shown. Solid line denotes the c_{enc} curve.

$$\frac{c_{wake}}{r\Omega} = 14.2 \left(\frac{a}{10^8 \text{ m}}\right)^3 \left(\frac{\rho}{900 \text{ kg m}^{-3}}\right) \tau. \qquad (18)$$

Attempting to find a rough description of the behavior, we study the possibility that the steady state is dominated by the factor yielding the largest minimum velocity dispersion.

According to Eqs. (16)–(18), c_{enc} is comparable to c_{imp} throughout Saturn's rings (assuming ε = constant), unless ρ is considerably below the density of water ice: $c_{enc}/r\Omega$ varies between 2 and 6 for $a = 70{,}000$–$140{,}000$ km if $\rho = 900$ kg m^{-3}. On the other hand, c_{wake} dominates c_{enc} unless τ is small; $c_{wake}/r\Omega \approx (5\text{–}40)\tau$ for the same distance range and density. Therefore, the easiest way to separate the three different factors is to use ρ as a free parameter and study several values of τ, as is done in Fig. 9. Notice that in Eqs. (16)–(18) the expected velocity dispersion scales in all cases in proportion to r; therefore simulation results for the chosen $r = 1$ m are readily applicable to other r's as well. Observed values are also collected in Table II.

In the absence of self-gravity ($\rho = 0$) increase of τ leads to a slightly reduced c_x, basically due to the less effective viscous gain as the particles' mean radial excursions between impacts are smaller. Equilibrium $c_x/r\Omega$ is reduced from about 3 to 2.5 for the studied τ range. For small nonzero ρ the gravitational forces are still insignificant and c_{imp} continues to dominate. If ρ is increased but τ is still small, c_{enc} exceeds c_{imp} while c_{wake} stays smaller; accordingly c_x starts to follow the c_{enc} curve. In Fig. 9a this is seen for $\tau = 0.1$, where c_x values follow the solid line corresponding to gravitational scattering due to encounters; the dotted line which corresponds to c_{wake} for $\tau = 0.1$ is always below the c_{enc} curve. These results agree with Ohtsuki (1992) who found that in low-τ systems self-gravity is unimportant if the collisions alone are able to maintain velocity dispersion exceeding v_{esc}.

For larger τ's and thus for larger surface mass densities, c_{wake} exceeds c_{enc} for certain ρ and accordingly c_x values start to follow the c_{wake} lines. This is seen in Fig. 9a for $\tau = 0.25$ and 0.39. However, for very large densities ($\rho \approx 2700$ kg m^{-3}), the velocity dispersion becomes considerably larger than predicted by Eq. (18). The same takes place for $\tau = 0.1$; c_x starts to deviate from the c_{enc} curve. These deviations follow from the formation of gravitational particle groups which efficiently scatter the other particles. Even for somewhat smaller ρ the wakes continuously form transient condensations which survive for several orbital periods: this probably explains why Q_T starts to exceed 2 (see the values for $\tau = 0.25$). Examples

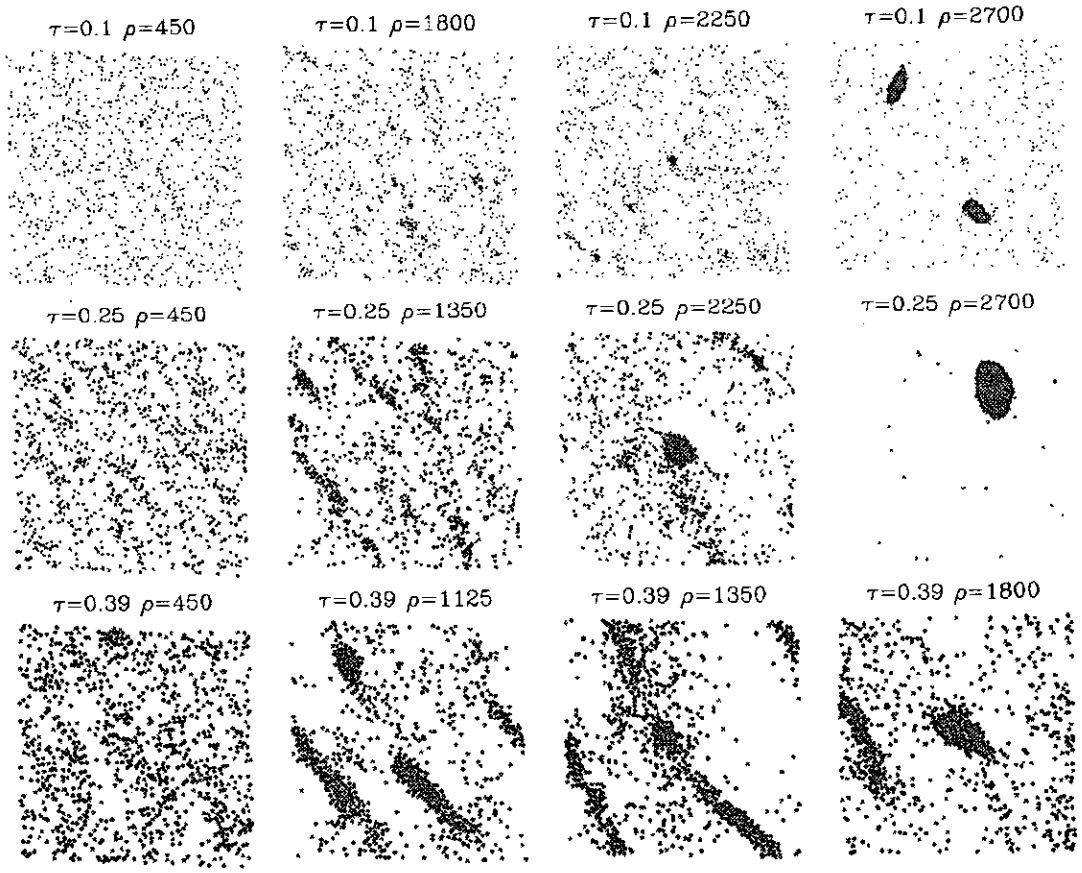

FIG. 9c. Examples of the particle positions at the end of simulations of Fig. 9a (after 20 orbital revolutions). The two groups seen for $\tau = 0.1$, $\rho = 2700$ kg m^{-3} formed after 10 orbital periods, while that for $\tau = 0.25$ formed already after 2 periods. All other clumps are transient.

of the particle positions at these runs are displayed in Fig. 9c, illustrating both the increased tendency to wake formation as ρ and τ are increased and the eventual clumping of wakes into distinct particle groups.

Figure 9b shows in greater detail the simulation results for small ρ's, together with theoretical estimates based on Hämeen-Anttila and Salo (1993). Theoretical curves take into account the simultaneous influence of collisions and gravitational encounters, as well as the increased mean vertical field, but they do not include the formation of collective wakes. For this reason they fail to reproduce the increased velocity dispersion for large ρ values. However, they yield very accurate steady-state values for the nongravitational case, and also give a qualitatively correct description for the drop of equilibrium velocity dispersion as ρ is slightly increased from zero. This decrease follows from the gravitational acceleration before impacts, leading to enhanced energy dissipation (see also Lukkari and Salo 1984). For $\tau = 0.1$ in which case the collective effects are weak and the velocity dispersion is dominated by two-particle encounters and physical impacts, the theoretical curve gives good agreement for all ρ's which do not lead to aggregate formation.

The next series of simulations (Fig. 10) modeled the evolution for various τ's while the internal density was fixed to that of solid ice, $\rho = 900$ kg m^{-3}. Values larger than $\tau = 0.6$ were not simulated as the small L/λ_{cr} would then underestimate c_x significantly (see Table III). According to Fig. 10a, in the gravitating case the increased τ leads to strongly increased c_x. At the same time fluctuations in velocity dispersion strengthen (see the error bars). Both c_x and c_y grow in a similar fashion (c_y denotes the dispersion of tangential velocities relative to the mean shear, $\dot{y} + 1.5\Omega x$), while in c_z the increase is smaller, which leads to practically constant $c_y/c_x \approx 0.5$ while c_z/c_x is strongly reduced. As noted earlier, impact frequency is much higher than in the nongravitating case. It also rises in a nonlinear fashion as compared to the linear τ-dependence in the former case. The frame in the lower left-hand corner displays c_x in dimensionless units; after being determined by encounters for $\tau \leq 0.2$, c_x first attains values around $Q_T \approx 2$ and then exceeds it for $\tau \geq 0.4$. This overshooting most probably follows from the increased tendency for particle grouping, some signs of which are visible in Fig. 10b, showing the positional plots. However, groups manifest as density enhancements in wakes, not

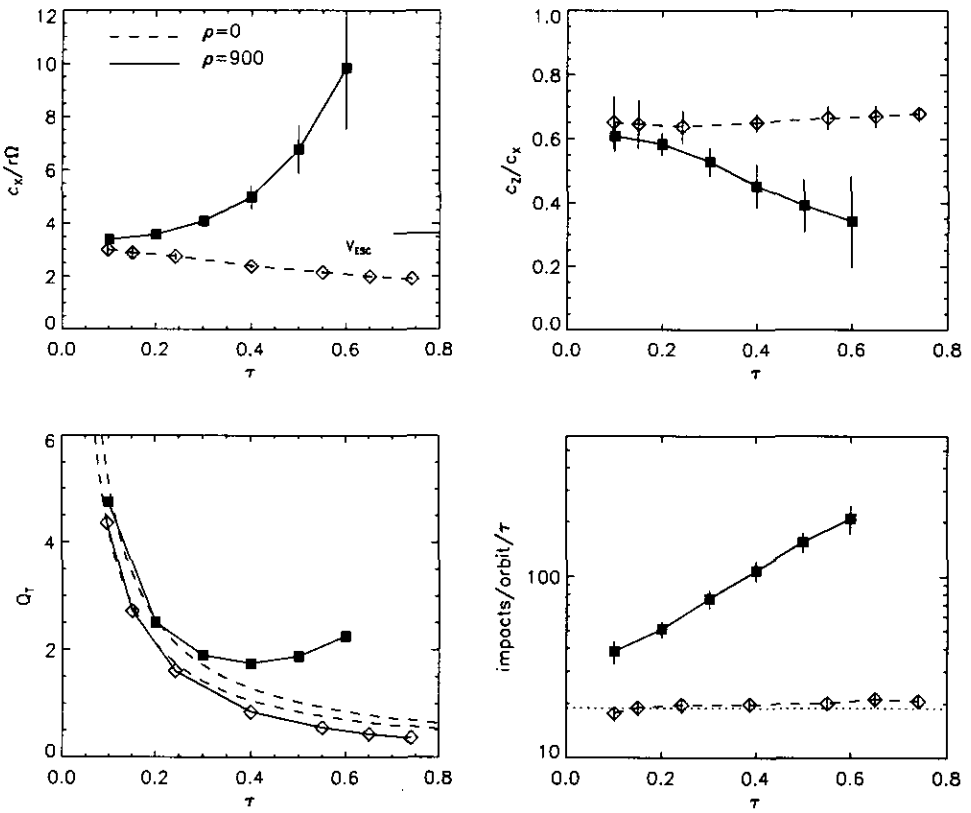

FIG. 10a. Dependence of equilibrium properties on τ, with (ρ = 900 kg m^{-3}, solid lines and filled symbols) and without gravitational forces (ρ = 0, dashed lines and open symbols). In the plot for impact frequency the dashed line stands for the relation $6\pi\tau$ impacts/particle/orbital revolution. In the frame displaying Q_T (c_r is normalized to c_{cr} of the self-gravitating runs), the upper dashed curve stands for the escape velocity and the lower curve for $3\Omega r$. In each run L = 112 m and the increased τ corresponds to larger N in the range 400–2400. In terms of surface density, τ = 0.6 corresponds to Σ = 720 kg m^{-2}.

as separate stable structures as in the high-ρ experiments (compare Fig. 10b with Fig. 9c). Although the wake structure is not readily apparent in the positional plots for $\tau \leq 0.2$, it can be clearly seen in the autocorrelation of particle positions.

5. INFLUENCE OF ELASTIC PROPERTIES

All the above experiments were performed with a constant coefficient of restitution, $\varepsilon = 0.5$. As the amount of dissipation depends strongly on ε, other choices were also explored. In addition to various constant values of ε, two different functional forms of velocity-dependent elasticity were studied. According to the laboratory measurements of Bridges *et al.* (1984), the coefficient of restitution for ice particles at low temperatures can be written in the form

$$\begin{aligned} \varepsilon(v) &= \max[(v/v_c)^{-0.234}, 0.25] \quad (v > v_c) \\ &= 1 \quad (v \leq v_c), \end{aligned} \tag{19}$$

where v is the perpendicular component of the impact velocity and v_c is constant. According to the Bridges *et al.* measurements $v_c \approx 0.01$ cm/sec; this value is denoted by v_B in the subsequent discussion. This functional form, which predicts fairly inelastic impacts with $\varepsilon \leq 0.5$ even for moderate impact velocities of a few mm/sec, has been widely studied in simulations (e.g., WT, Salo 1992a, 1992b, Hänninen and Salo, 1994). Later Hatzes *et al.* (1988) performed improved laboratory experiments (lower temperature, reduced amount of frost in particle surfaces) which yielded considerably less inelastic behavior. Recently, Dilley (1993) has proposed theoretical models fitting accurately both the velocity and the size dependence of the Hatzes *et al.* measurements in the range $v < 2$ cm/sec, 2.5 cm $< r <$ 20 cm. According to Dilley (1993),

$$\begin{aligned} \varepsilon(v) &= e^{-\pi\xi/\sqrt{1-\xi^2}}, \\ \xi &= \xi_0 v^p (1 + r_1/r_2)^{0.2} (1 + (r_1/r_2)^3)^k (r_1/2.5\text{ cm})^{-3k-0.2}, \end{aligned} \tag{20}$$

where r_2 and r_1 are the radii of the larger and the smaller

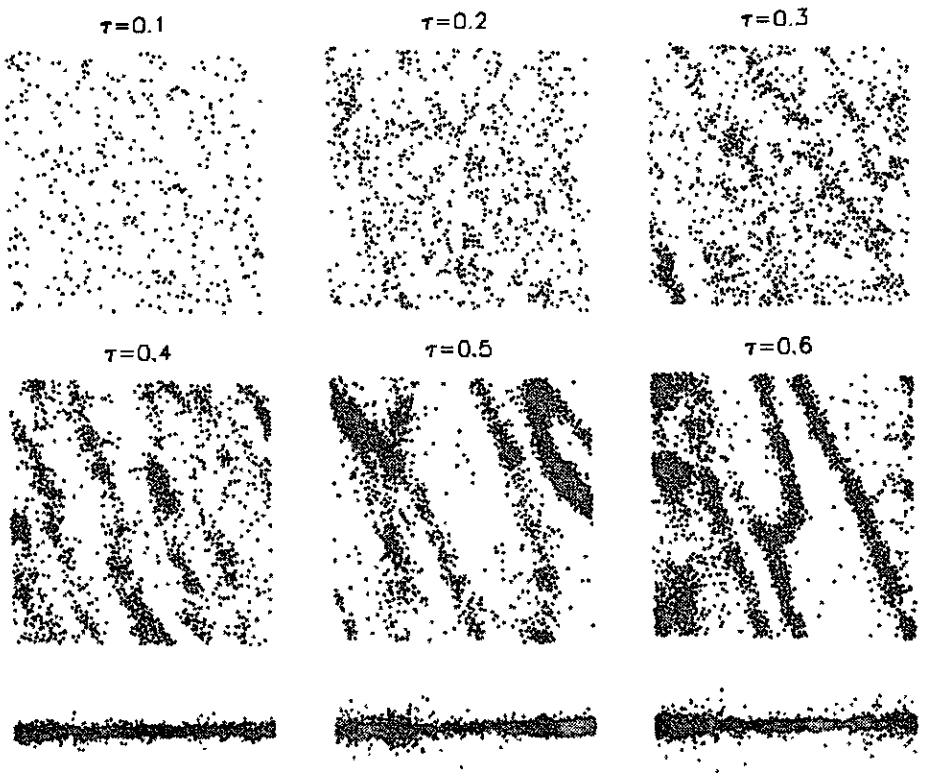

FIG. 10b. Particle positions at the end of the gravitating simulations of Fig. 10a. In each case $L_x = L_y = 112$ m and the different τ's correspond to different N.

colliding particle, respectively, and the exponent k describes the mass dependence (not determined by the Hatzes *et al.* experiments). Impact velocity is expressed in cm/sec. The parameters ξ_0 and p depend on the properties of the ice spheres; for example, $\xi_0 = 0.16$ and $p = 0.65$ for the Hatzes *et al.* measurements at the temperature $T = 133$ K with thin frost. Scaled to 1-m particles (with $k = 0$) these models imply that ε is in the range 0.6–0.8.

Figure 11 displays results of simulations performed for various values of constant ε. In the nongravitating case, the equilibrium velocity dispersion is on the order of a few times $r\Omega$ (increases monotonically with ε), unless ε exceeds critical value $\varepsilon_{cr}(\tau)$, in which case steady state is no longer possible. In Fig. 11a, $\varepsilon = 0.65$ still leads to steady state while for $\varepsilon = 0.70$, particle eccentricities and inclinations grow continuously with time (indicated by dashed line). This agrees with the theoretical predictions; according to Goldreich and Tremaine (1978) $\varepsilon_{cr} \approx 0.69$ for $\tau = 0.4$, while Hämeen-Anttila (1984) gives $\varepsilon_{cr} \approx 0.72$. In the case of self-gravity the behavior is different for small ε; the minimum of c_x is obtained for $\varepsilon \approx 0.6$–0.65, with stronger dissipation leading to *larger* velocity dispersion. This again follows from the strong tendency for particle grouping to enhance gravitational scattering (see Fig. 11c). The particle grouping is also evidenced by the strongly enhanced impact frequency (Table IV). The critical ε is somewhat increased to ≈ 0.75. Notice that in the self-gravitating case $c_z/r\Omega$ is practically independent of ε, corresponding to an effective thickness $H \approx 6r$. Without self-gravity, equilibrium corresponds to a practically monolayer state.

In the case $\varepsilon = \varepsilon(v)$ the equilibrium state is determined by the parameters of the elasticity model (see Salo *et al.* 1988). For example, with the Bridges model, Eq. (19), velocity dispersion in the absence of self-gravity scales proportional to v_c if $v_c \gg r\Omega$, while for small v_c velocity dispersion is proportional to $r\Omega$ (see Salo 1991, where this model is studied for $\tau = 1$ and the equilibrium velocity dispersion vs v_c/v_B is displayed in log–log scale). The inclusion of self-gravity leads to a qualitatively similar behavior as in the case ε = constant, so that larger dissipation enhances velocity disperion with the minimum being attained for $v_c \approx 2v_B$.

Figure 11b depicts all the experiments with varying elastic properties, displaying the radial velocity dispersion in the gravitating case versus that for nongravitating case. Self-gravity influences the equilibrium state significantly via formation of wakes only if the corresponding nongravitating simulation yields $c_x/r\Omega \leq 5$, regardless of the details of the elasticity model. This is the case if $\varepsilon =$

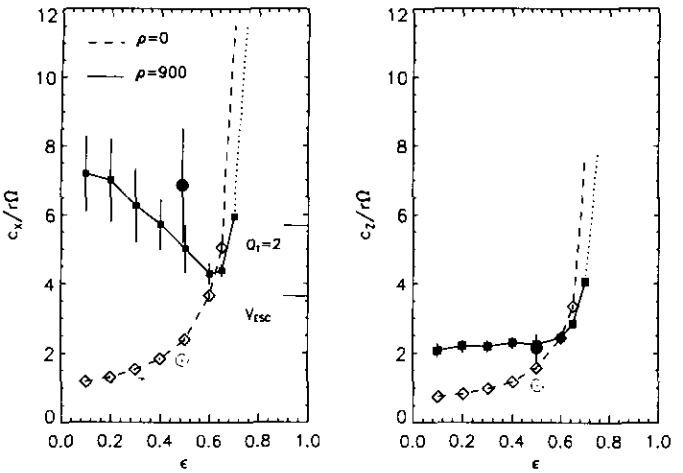

FIG. 11a. Results of simulations where constant coefficient of restitution is studied, both for gravitating (ρ = 900 kg m^{-3}) and for nongravitating particles (ρ = 0). Other parameters of the simulation were fixed: a = 100,000 km, r = 1 m, τ = 0.4, and N = 1000. Circles stand for simulations with spinning particles, with coefficient of friction ε_t = 0.5. Filled symbols stand for gravitating and open symbols for the nongravitating case.

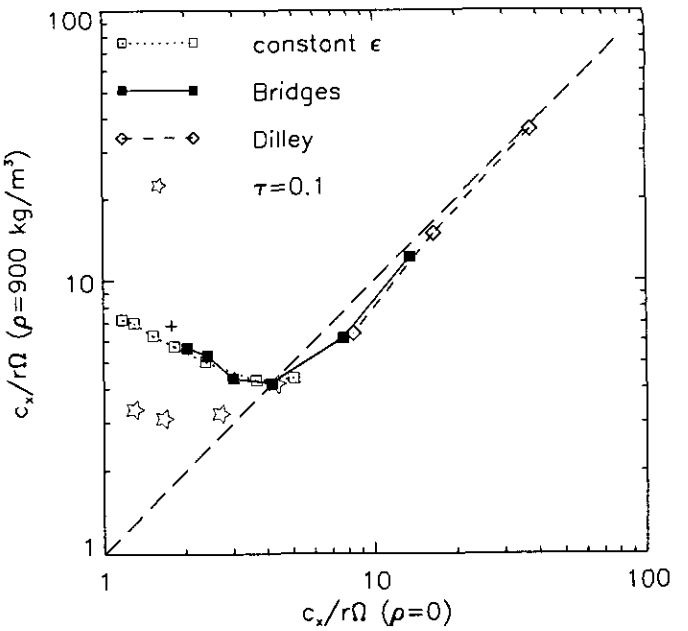

FIG. 11b. Radial velocity dispersion in the gravitating simulation vs that in the corresponding nongravitating experiment. Simulation results of Fig. 11a (ε = 0.1–0.65) are collected in the same frame as well as experiments with velocity dependent elasticity models (v_c/v_B = 0.25–10 in Bridges-type formula, Eq. (19); three different Dilley models, Eq. (20), are studied: ξ_0 = 0.16, p = 0.65 [thin frost, T = 133 K], ξ_0 = 0.25, p = 0.43 [thick frost, T = 127 K], ξ_0 = 0.34, p = 0.36 [thick frost, T = 210 K]). The straight dashed line stands for $c(\rho = 900) = c(\rho = 0)$. Cross denotes the simulation with spinning particles and tangential friction ($\varepsilon = \varepsilon_t$ = 0.5). Asterisks denote simulations with τ = 0.1.

constant ≤ 0.6 or if $v_c \leq 2v_B$ in Eq. (19). On the other hand, all the Dilley-type models predict such a large velocity dispersion that inclusion of self-gravity does not significantly affect the equilibrium. However, according to Fig. 9 the limit $c_x/r\Omega \leq 5 \approx c_{wake}$ scales

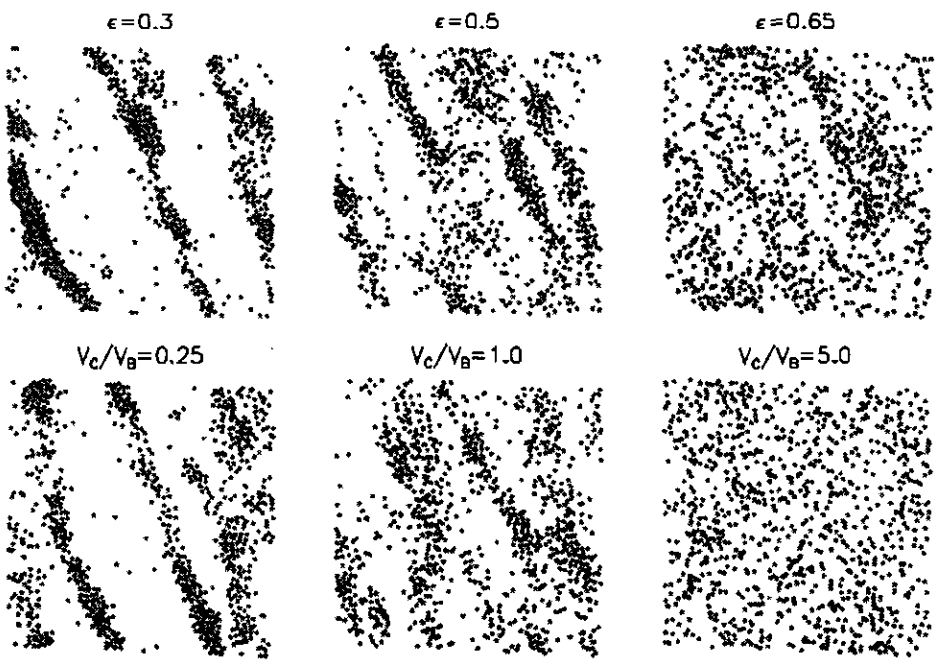

FIG. 11c. Examples of particle positions at the end of the simulations with various constant values of ε (upper row) as well as with the velocity dependent model, Eq. (19) (lower row).

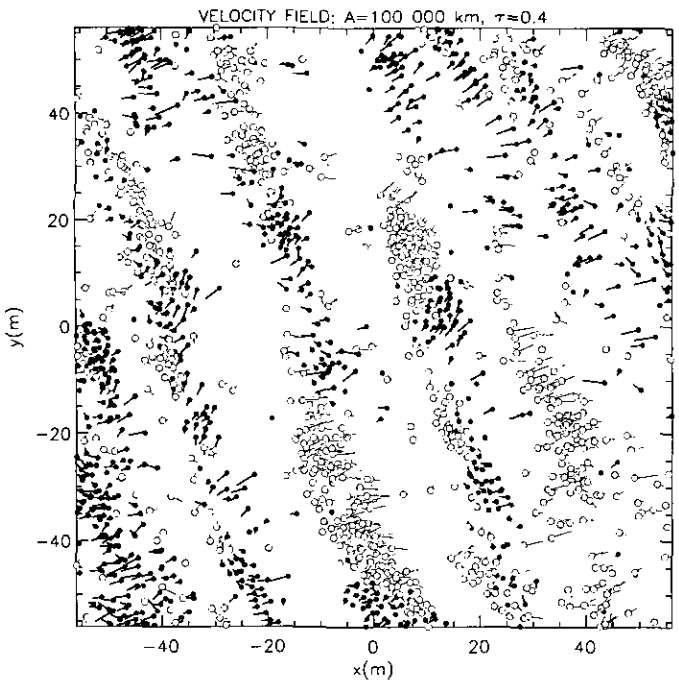

FIG. 12. Velocity field in the simulation of Fig. 10, with $\tau = 0.4$. Tails indicate the direction of the particle, with the lengths corresponding to movement in 0.05 orbital revolutions. For clarity, particles with positive radial velocity are shown by filled symbols. The circular orbital velocity at the position of the particle has been subtracted from the tangential velocities.

proportional to the parameters ρ and τ determining the surface density; therefore for larger τ's self-gravity would be important also for more elastic impacts (the same is true for larger semimajor axes; see the next section). Also, for smaller τ's, the maximum velocity dispersion for the self-gravity to be important depends rather on $c_{\rm enc}$. This was verified in a few additional simulations for $\tau = 0.1$, which are also displayed in Fig. 11b.

Some experiments with tangential friction were also carried out, in which case the particle spins were taken into account. The value $\varepsilon_t = 0.5$ was used for the coefficient of friction. Results of the two experiments with $\varepsilon = 0.5$, both for $\rho = 0$ and for $\rho = 900$ kg m^{-3}, are also shown in Fig. 11a (circles). As friction enhances energy dissipation, the equilibrium velocity dispersion in the nongravitating case is somewhat reduced, by about 30%. In the gravitating case, inclusion of friction leads to an *increase* in velocity dispersion, mainly via increased c_x and c_y. This again follows from the enhanced tendency for grouping; for example, the wake structure in the simulation with $\varepsilon = 0.5$, $\varepsilon_t = 0.5$ is very similar to that in the case $\varepsilon = 0.3$, $\varepsilon_t = 0$.

An interesting detail is the behavior of the mean spin. According to theoretical studies (e.g., Araki 1991, Salo 1987a, Hämeen-Anttila and Salo 1993) the mean spin, $\langle\omega_z\rangle$ is fairly insensitive to different parameters including τ and ε_t, being about (0.30–0.35) Ω in the same sense as orbital rotation. Also, inclusion of the mean vertical field does not affect its value. Our result from the present simulations, $\langle\omega_z\rangle/\Omega \approx 0.36 \pm 0.02$ for $\rho = 0$, is consistent with these predictions as well as with the earlier simulations performed with a totally different code which did not use the local method (Salo 1987b). However, in the present run with $\rho = 900$ kg m^{-3}, $\langle\omega_z\rangle/\Omega$ is significantly larger, $\approx 0.66 \pm 0.09$. This suggests that the formation of wakes, not taken into account in the above-mentioned theoretical treatments, significantly affects the distribution of impact directions and velocities in a manner that enhances $\langle\omega_z\rangle$. Another difference in the behavior of rotating gravitating particles is in the ratio of energies stored in the random motions and in particle spins, $E_{\rm rot}/E_{\rm kin} = \frac{2}{5}\langle(r\omega)^2\rangle/c^2$. In the nongravitating experiments this ratio rapidly attains a steady-state value, the dispersion of spin velocities following the evolution of mutual impact velocities which are proportional to the random velocity dispersion. In the present nongravitating experiment $E_{\rm rot}/E_{\rm kin} \approx 0.11$, in agreement with theoretical studies of dense rings (e.g., Hämeen-Anttila and Salo 1993) and also fairly close to the approximation $2\varepsilon_t/(14 - 5\varepsilon_t) \approx 0.09$ found for a rarefied disk (Salo 1987a). However, in the corresponding gravitating run $E_{\rm rot}/E_{\rm kin}$ is only about 0.04. The smaller ratio for the self-gravitating case may be due to the fact that the local velocity dispersion experienced by particles is actually smaller than the global value studied so far.

Indeed, most of the increase in the velocity dispersion for the self-gravitating experiments comes from the differences in the systematic motions between the adjacent wakes. This is illustrated in Fig. 12, showing the particle's velocity field (with systematic shear subtracted) in the simulation with $\tau = 0.4$, $\varepsilon = 0.5$ (see Fig. 10b). For clarity, particles with positive and negative radial velocities are distinguished. The largest velocities are observed in the regions between the wakes. Figure 13 displays in a more quantitative manner the difference between the global and local velocity dispersion in the self-gravitating experiments of Figs. 10 and 11, the former showing the rms values over the whole calculation area. The latter is calculated for each particle separately, relative to the local mean velocity (from the 10 nearest particles) and then averaged over the system. Typically, local c_x and c_y are both approximately constant for different values of ε and τ, in spite of the large difference in the global dispersion. For c_z the difference between local and global values is smaller, but still significant when ε is small or τ large; local ratios c_z/c_x can be much larger than the global value, and they rise toward unity when τ is increased. In the nongravitating case the differences between local and global velocity dispersions vanish. Also, the earlier difference in the

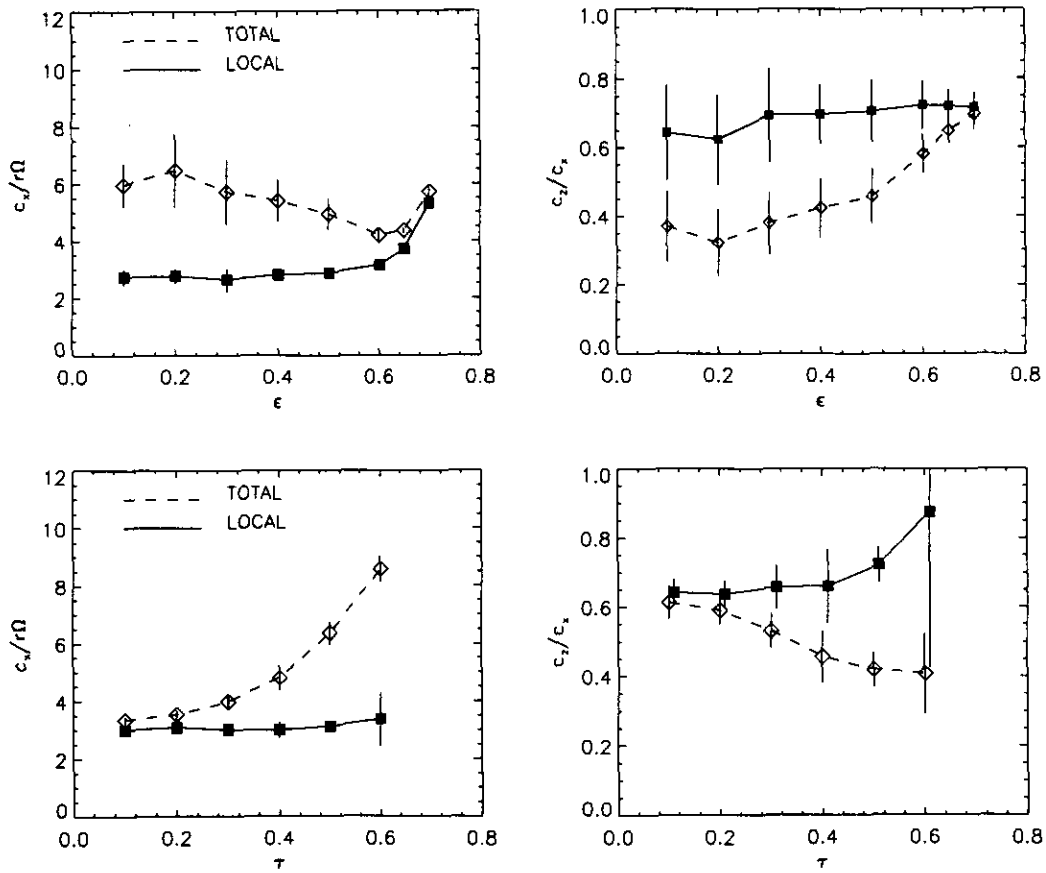

FIG. 13. Total and local velocity dispersion in self-gravitating simulations of Figs. 10 and 11. The local velocity dispersion was calculated for each particle from the motions of the 10 nearest particles, and then averaged over all particles. The total value is the rms value for the whole system, thus including the streaming motions of the wakes with respect to each other.

$E_{\rm rot}/E_{\rm kin}$ between gravitating and nongravitating rotating particles disappears if local dispersions are used.

6. INFLUENCE OF RADIAL DISTANCE

As the significance of self-gravity increases with reduced differential rotation, a series of experiment was performed by varying the saturnocentric distance between a = 70,000–140,000 km, while keeping the particle density, surface density, and elasticity constant. Figure 14 displays the particle positions achieved at the end of these simulations while Fig. 15 shows the corresponding radial velocity dispersions. Readily visible in Fig. 14 is the increased amplitude and separation of wakes as a is increased. Simultaneously, the clumpiness of the wakes strengthens and at a = 140,000 km the system rapidly forms a massive aggregate containing almost all particles. Already for a = 130,000 km this tendency is very strong and practically destroys the wake structure. In the velocity dispersion plot the formation of transient clumps manifests with $Q_{\rm T}$ values exceeding 2. Notice also that the c_x values for larger a's are likely to be underestimated due to small size of the simulation region (see Table V). Smaller values of τ were also simulated (τ = 0.1 in Fig. 15); in this case $c_x \approx v_{\rm esc}$ as gravitational encounters dominate over collective wake formation.

As the vertical velocity dispersion c_z is proportional to c_x, Fig. 15 also indicates strongly enhanced geometric thickness for the outer parts of Saturn's rings. The observed $H/r \approx 2.7c_z/r\Omega \approx 1.1c_x/r\Omega$. Therefore, the numerical values of the ordinates correspond roughly to the effective thickness obtained with 1-m particles, whereas for larger sizes they have to be multiplied by (r/1 m).

The behavior at the distance a = 140,000 km was further studied in additional experiments with smaller τ's. All the displayed examples (Figs. 16a and 16b) lead to a formation of stable aggregates; in the case τ = 0.2–0.4 the formation occurs within the first few orbital revolutions, with the initial condensations rapidly coalescing into a single aggregate containing practically all simulation particles. For example, the clumps seen in the frame T = 2 for τ = 0.3 can all still be distinguished in the aggregate of T = 5 frame if individual particles are followed. In the case of smaller τ's, the timescale for aggregate formation is

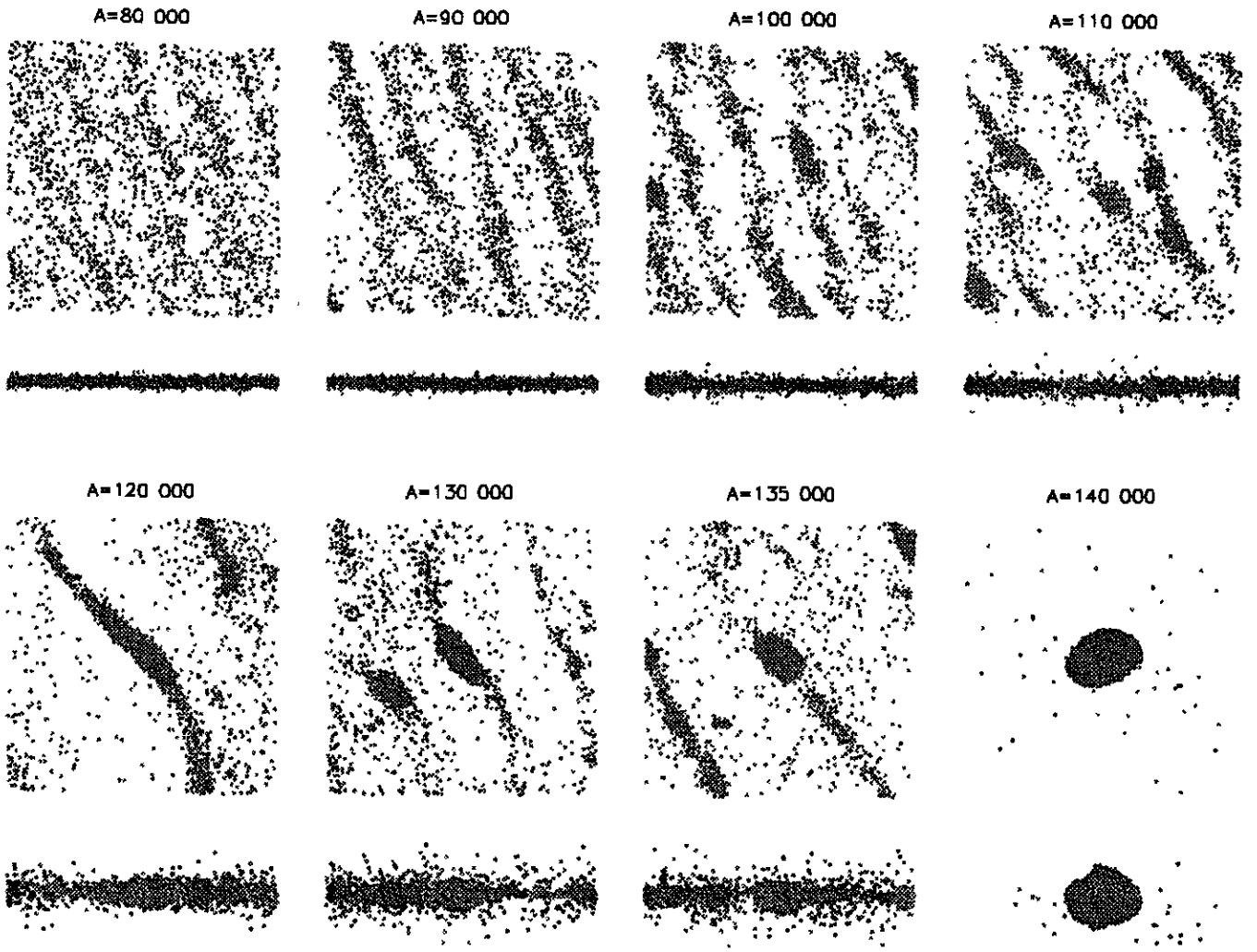

FIG. 14. Particle positions at the end of simulations performed for various Saturnocentric distances with $\tau = 0.4$, $\varepsilon = 0.5$, and $\rho = 900$ kg m^{-3}. The duration of each simulation was 15 orbital revolutions. In each case $N = 1600$, and $L_x = L_y = 112$ m.

longer, several tens of orbital periods (for example, the group seen for $\tau = 0.1$ grows continuously to the end of the simulation; also, its growth is evidently slowed down by clearing the radial lane where it resides). Also, several stable groups can coexist in the simulation region ($\tau = 0.05$). The coefficient of restitution also affects the grouping tendency: for $\varepsilon = 0.1$ several aggregates form very rapidly. An interesting detail is the mutual interaction of these groups; although they retain their identity there is a continuous exchange of particles. For example, the particles residing in the largest aggregate of the $T = 80$ frame were distributed between all the five groups seen in $T = 40$.

One important point concerning the displayed aggregate formation deserves mentioning. Although the above series of simulations for $a = 140{,}000$ km leads in every case to a rapid formation of aggregates, the limiting distance for the onset of aggregate formation is not very sharply defined. Namely, altogether 10 experiments (with duration of 10 orbital periods) were performed for $a = 140{,}000$ km, $\tau = 0.4$, and $\varepsilon = 0.5$, with slightly different simulation parameters. Out of these, 5 experiments failed to form any stable aggregates during the admittedly short duration of these simulations. Even different seeds for the random number generator used in the creation of initial particle positions can make the difference between accretion and nonaccretion. Nevertheless, in a similar series for $a = 150{,}000$ km, all experiments led to rapid aggregate formation. We are currently studying in more detail the dependence of particle grouping on distance and on the model for (in)elasticity (Lukkari and Salo, in preparation).

7. PARTICLE GROUPS

It is interesting to compare the results of the experiments leading to accretion with the semianalytical criteria

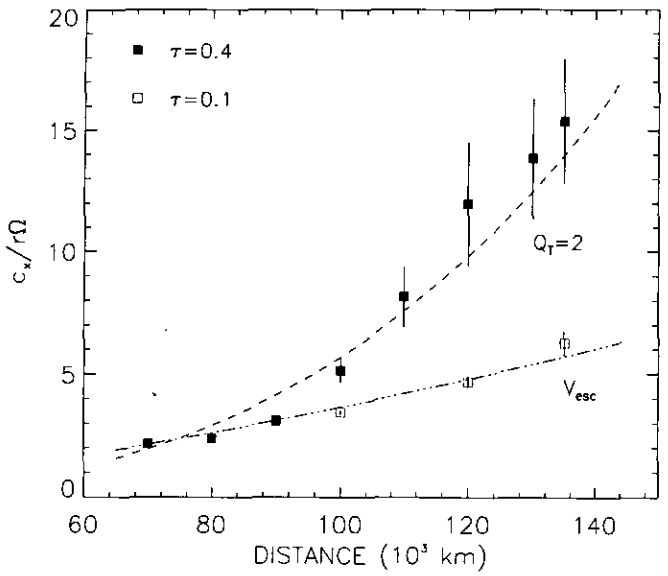

FIG. 15. Radial velocity dispersions in the experiments from Fig. 14. Symbols stand for observed values, while dashed and dashed–dotted curves indicate the $Q_T = 2$ relation (for $\tau = 0.4$) and the escape velocity from the particle surfaces, respectively.

derived by Ohtsuki (1993, see also Canup and Esposito 1995), based on the numerical three-body integrations of particle orbits in planetary rings. According to Ohtsuki (1993), the possibility of accretion is determined by the ratio of the sum of the particle radii to the Hill radius, $r_p = (r_1 + r_2)/R_{Hill}$, where $R_{Hill} = a(m_1 + m_2)^{1/3}/(3M)^{1/3}$; for $r_p \leq \frac{2}{3}$ particles are inside their Hill surface and accretion is the typical outcome of impact unless ε is close to unity, while for $r_p \geq 1$ accretion is completely suppressed. For intermediate values $\frac{2}{3} < r_p < 1$ particles extend partially out of their mutual Hill surface, and accretion is possible but quite difficult. The condition $r_p \leq 1$ is identical to the Weidenschilling *et al.* (1984) limit for synchronously rotating particles feeling a net attraction toward each other, as well as with the accretion condition adopted in Longaretti's (1989) analytical study of the evolution of particle size distributions in Saturn's rings.

For Saturn's rings the scaled radius of the particle pair can be written as

$$r_p = 0.77 \left(\frac{\rho}{900 \text{ kg m}^{-3}}\right)^{-1/3} \left(\frac{a}{10^8 \text{ m}}\right)^{-1} \frac{1 + \mu^{1/3}}{(1 + \mu)^{1/3}}, \quad (21)$$

where μ is the mass ratio of the impacting particles. For identical particles with $\rho = 900$ kg m^{-3} this formula yields r_p(100,000 km) = 1.22 and r_p(140,000 km) = 0.87, with the limit $r_p = 1$ being attained for $a \approx 122{,}000$ km. This is consistent with the observed accretion at $a = 140{,}000$ km, but as $r_p > \frac{2}{3}$ the accretion probability in an individual impact should be small; according to Ohtsuki, probability is already below 5% for $r_p = 0.74$ and decreases rapidly as r_p increases. Apparently the strong observed tendency for particle groupings is due to the high impact frequency, so that even a small capture probability is sufficient for numerous simultaneous particle groupings. Another factor that helps accretion in a realistic many-particle case is the fact that as particle groups are formed, the effective mass ratio in impacts between the existing group and an impacting particle is increased. For example, if we assume that a spherical aggregate contains about 200 particles, with a filling factor close to the three-dimensional limit of $\pi/\sqrt{18} \approx 0.74$, the effective value of r_p for an attachment of an individual particle on the surface of the aggregate would rise to r_p(140,000 km) = 0.71. However, this underestimates the actual attainable r_p values as the true filling factor is always less than the maximum. Thus, in principle, accretion seems easier in the case of unequally sized particles as the small particles can then fill the voids between the large ones, thus increasing the volume density. An example of this is shown in Fig. 17, comparing an aggregate formed at $a = 130{,}000$ km in the case of nonidentical particles and that in the previous $a = 140{,}000$ km, $\tau = 0.4$ experiment of identical particles. The size distribution here is the same power law which was studied by Salo (1992b).

Some attempts were made to determine the r_p values corresponding to the attachment of new particles to the aggregates seen in the various positional plots. For that purpose the density profiles of the aggregates were measured. The calculation of the volume density was performed with Monte Carlo method: each particle was filled with 100 random mass elements whose distance from the group center was tabulated. In the case of groups containing just a few tens of particles this is more accurate than using the locations of the particle centers. Figure 18 provides an example of volume density and r_p profiles for the aggregates of Fig. 17. The results of several other experiments are collected in Tables VI and VII, displaying group sizes and properties in various simulation systems displayed in Figs. 9c, 11c, 14, and 16. The group size was determined by fitting an ellipsoid to the particle positions and measuring its minor axis in the equatorial plane; R_{group} is defined to be twice the dispersion in this direction. Although rather arbitrary, this measure has the advantage that it can also be applied to the cases where groups are not isolated but represent denser portions of wakes (transient groups in Table VII). The quantity N_{group} denotes the number of particles within distance R_{group} from its center, being often less than one-half of the total number of particles in the group, depending on its shape. Volume density indicates the mean filling factor inside R_{group}.

According to Table VI, the rapidly formed aggregates

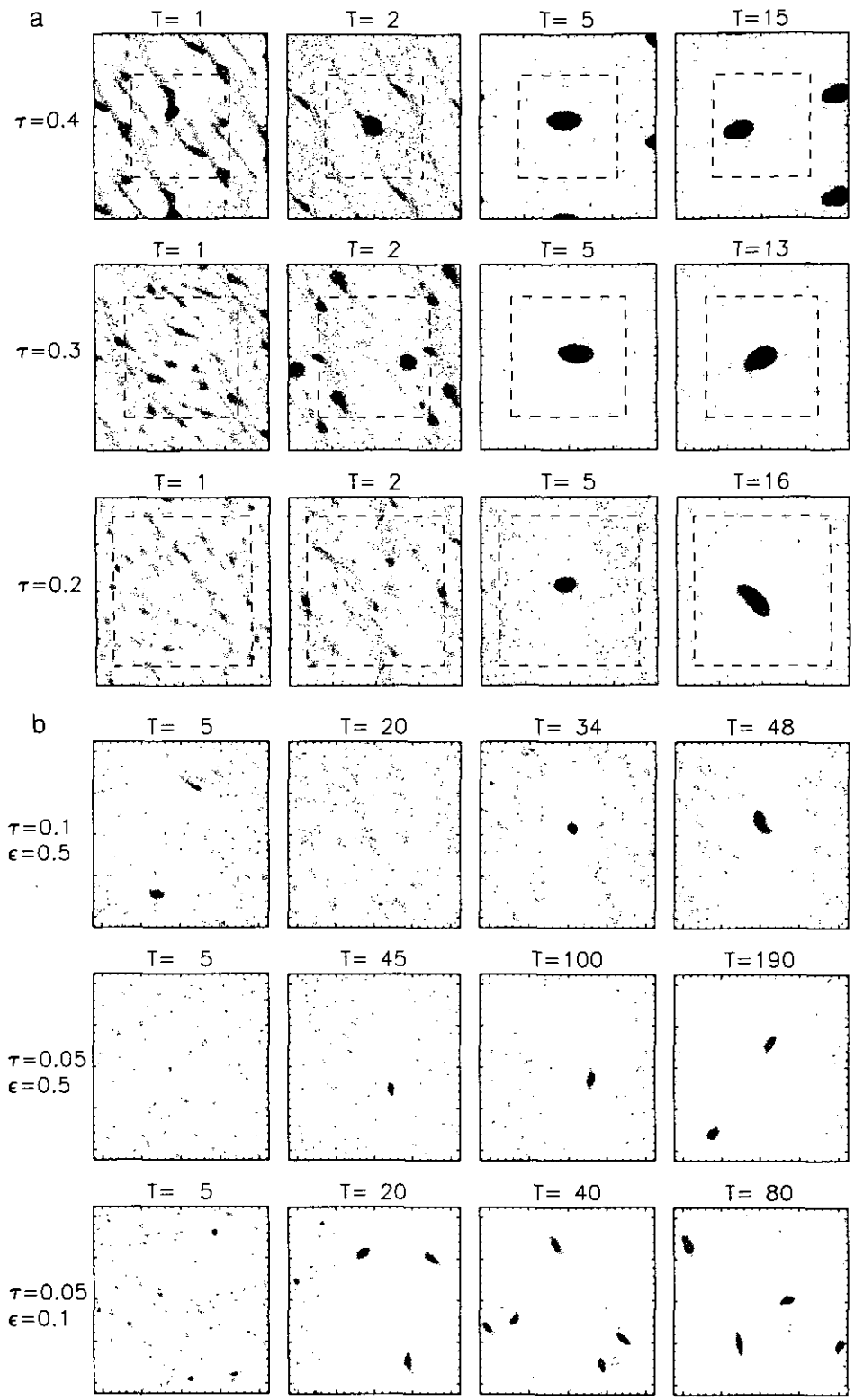

FIG. 16. Examples of particle groups in simulations for a = 140,000 km, for various times during the simulation (in units of orbital revolutions). In (a) each frame shows a 100 × 100 m region, while the actual calculation cell is denoted by a box. In each case 1600 particles were simulated and optical thickness was varied by changing the size of the calculation cell. The coefficient of restitution $\varepsilon = 0.5$. In (b) the calculation cell is fixed (L = 112 m), and N = 1600 for $\tau = 0.1$, while N = 800 for $\tau = 0.05$.

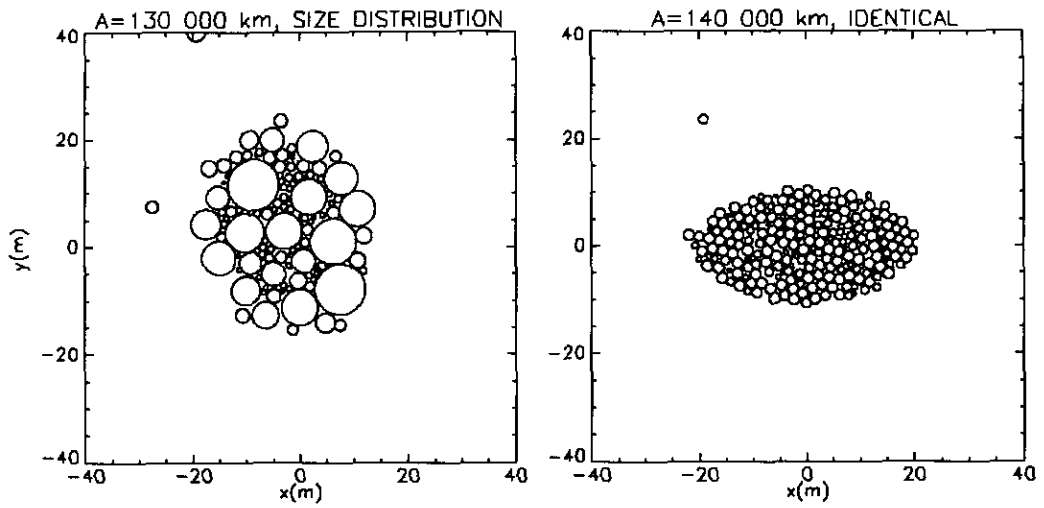

FIG. 17. Comparison between simulations with a power-law size distribution ($dN/dr \propto r^{-3}$ for $0.50 < r < 5$ m) and with identical particles. A slice of the simulation system through the equatorial plane is shown. Note that the experiment on the left corresponds to a = 130,000 km, while for that on the right, a = 140,000 km. In both cases, Σ = 480 kg m^{-2}.

in Fig. 16a all have $r_p \approx 0.7$, in accordance with Ohtsuki's value of $\frac{2}{3}$. Similar values are observed for the stable aggregates seen in Fig. 9c, as well as in the size distribution experiment of Fig. 17. However, for smaller τ's in Fig. 16b, r_p values in the range 0.77–0.93 are observed, indicating that growth is possible even for $r_p > \frac{2}{3}$. It is also worth remembering that the above values refer to minor-axis values, with the major axis of the groups extending sometimes well outside the Hill radius (for example, with τ = 0.2 in Fig. 16a, r_p = 1.2 for the outermost particles). Also, in the simulations with transient clumping of wakes (Table VII), r_p values in the range 0.8–0.9 are sometimes observed. Apparently, in these cases the perturbation from the adjacent wakes prevent the collapse of the clumps into separate groups.

For comparison, Table VI also shows the properties of the aggregate formed in the previous A-ring simulation with a size distribution (Salo 1992b). In these old simulations the particle overlap at the end of the experiment was already sizable, leading to about 5% enhancement in the aggregate density. However, comparison with the present size-distribution experiment, where overlaps are totally insignificant, shows that numerical deficiencies were not responsible for the stability of the groups observed earlier.

8. DISCUSSION AND SUMMARY

As we have seen, an extensive numerical survey of the effects of self-gravitation in collisional disks of identical particles has been performed, here concentrating deliberately on the parameter values most appropriate for Saturn's rings. The present experiments complement the size-distribution experiments briefly reported by Salo (1992b) by considering a much larger range of optical thicknesses, radial distances, and elasticity models, as well as by exploring the different domains where gravitational encounters and the collective Julian–Toomre wakes are likely to be important. Also, the formation of particle groups was now followed in some detail.

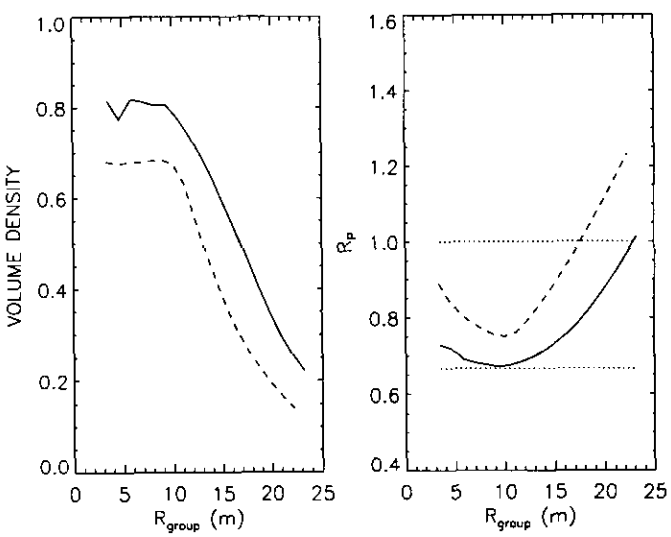

FIG. 18. On the left, the volume density of the aggregates of Fig. 17 are shown, as a function of the distance from the center (mean volume density within this distance). The solid line stands for the case with a size distribution, while the dashed line refers to the aggregate composed of identical particles. On the right, corresponding r_p parameters are shown. The two vertical lines indicate r_p = 1 and $\frac{2}{3}$. In the case of the size distribution the r_p values correspond to an attachment of a 50-cm particle on the aggregate.

TABLE VI
Properties of Stable Particle Groups in Simulations

Distance (10^3 km)	ρ (kg m^{-3})	τ	R_{group}	N_{group}	Volume density	r_p	Comment
140	900	0.4	11.4	921	0.61	0.72	Fig. 16a
140	900	0.3	10.3	638	0.58	0.73	Fig. 16a
140	900	0.2	9.1	460	0.61	0.73	Fig. 16a
140	900	0.1	5.7	117	0.63	0.77	Fig. 16b
140	900	0.05	5.0	70	0.57	0.82	Fig. 16b
140	900	0.05	6.2	90	0.38	0.93	Fig. 16b $\varepsilon = 0.1$
100	2700	0.25	7.9	315	0.66	0.70	Fig. 9c
100	2700	0.10	6.5	157	0.56	0.76	Fig. 9c
130	900	0.25	13.1	648	0.68	0.70	Size distribution: Fig. 17
128	900	0.25	12.2	390	0.77	0.69	Size distribution: Salo 1992b

Note. The properties of stable particle groups seen at the end of various simulations corresponding to different saturnocentric distances, particle internal densities, and system optical thicknesses. The group size R_{group} refers to the minor-axis radii in the equatorial plane and N_{group} is the number of particles within this radius. The cumulative volume density was determined by the Monte Carlo method explained in the text, and r_p stands for the radius of the group + particle scaled by the Hill radius (Eq. (21)), calculated by using R_{group} and N_{group}. The figure displaying the particle positions is indicated in the last column. Unless otherwise indicated, $\varepsilon = 0.5$.

Our experiments with various methods for approximating the self-gravity emphasize that the inclusion of all three force components is essential. If only the mean vertical field is considered, as in WT and in Salo (1991b), gravity leads to the reduction of velocity dispersion and vertical thickness, a result that is not reproduced by the present, more realistic calculations, where both mutual encounters between particles and collective wake formation lead to a much increased velocity dispersion. The accurate modeling of wakes necessitates the use of a considerably larger number of particles, which leads to a strongly increased CPU consumption. However, numerical tests indicated that calculation regions of size $L \geq (2\text{–}3)\lambda_{cr}$ yield sufficiently accurate (10–15%) rough results for equilibrium velocity dispersions and for transient wake structures, implying that the presently attainable numbers of a few thousand simulation particles may be sufficient for modeling systems with $\tau \leq 0.6$.

According to the present simulations, four different domains can be distinguished in the behavior of self-gravitat-

TABLE VII
Properties of Transient Clumps in Simulations

Distance (10^3 km)	ρ (kg m^{-3})	τ	R_{group}	N_{group}	Volume density	r_p	Comment
100	900	0.4	5.6	42	0.24	1.58	Fig. 14
110	900	0.4	5.3	51	0.34	1.26	Fig. 14
120	900	0.4	5.9	110	0.54	0.94	Fig. 14
130	900	0.4	6.1	138	0.57	0.85	Fig. 14
135	900	0.4	6.9	204	0.62	0.78	Fig. 14
100	900	0.4	5.0	62	0.50	1.12	Fig. 11c: $\varepsilon = 0.3$
100	2250	0.1	3.8	21	0.35	1.08	Fig. 9c
100	2250	0.25	6.6	163	0.56	0.81	Fig. 9c
100	1800	0.4	5.3	91	0.61	0.88	Fig. 9c

Note. The properties of transient particle groups seen at the end of various simulations corresponding to different Saturnocentric distances, particle internal densities, and system optical thicknesses. The group size R_{group} refers to the minor-axis radius in the equatorial plane and N_{group} is the number of particles within this radius. The figure displaying the particle positions is indicated in the last column. Unless otherwise indicated; $\varepsilon = 0.5$.

ing rings. First, if the internal density ρ and/or surface density Σ are small, gravitational effects are rather insignificant, and the steady state is determined by collisions and is somewhat affected by the gravitational accelerations before impact. In simulations with a constant coefficient of restitution $\varepsilon \approx 0.5$, this implies an equilibrium velocity dispersion c_{imp} on the order of a few $r\Omega$, and an impact frequency of approximately 20τ impacts/particle/orbital revolution. With larger ρ and Σ two new possibilities arise: the velocity dispersion becomes dominated either by scattering in mutual two-particle encounters or else by scattering due to collective wakes. Typically, encounters dominate only at low optical depths $\tau \leq 0.1$. In both cases, the impact frequency is strongly enhanced, by factors of 2 and 6 for $\tau = 0.1$ and 0.5, respectively. Also, in the case of wake formation, the velocity dispersion shows strong fluctuations. Finally, a fourth kind of behavior is the formation of stable particle aggregates, preceded by the increased clumpiness of the wakes. In the case of small τ, increased ρ leads directly to aggregate formation.

The significance of gravitational forces depends crucially on the elastic model adopted. Especially for constant coefficients of restitution, the self-gravity is always significant and manifests itself by an increased velocity dispersion. Furthermore, if ε is close to zero, the tendency for temporary particle groupings becomes stronger, evidenced by the increased impact frequency and the clumpiness of the wake structure (see Fig. 11). On the other hand, with velocity-dependent ε, the system can attain an equilibrium velocity dispersion exceeding $r\Omega$ by a large factor. For example, this is the case according to the laboratory measurements by Hatzes *et al.* (1988) if these results are scaled to meter-sized particles with the theoretical formulas by Dilley (1993). In this case the influence of gravitational forces becomes totally insignificant and no wake structure is expected. However, it is very uncertain how well the current laboratory measurements of spherical solid ice balls are applicable to the physical conditions in the ring systems. For example, Dones and Porco (1989) have shown by light-scattering simulations that Julian–Toomre-type wakes would offer a natural explanation for the observed (see e.g. Franklin *et al.* 1987) azimuthal brightness variations in Saturn's A-ring. Indeed, the pitch angles in the present simulations with sufficiently large calculation regions, about 23° (as inferred from autocorrelation plots like Fig. 8), agree remarkably well with the observed brightness minimum occurring 24 degrees before the ansae (Dones *et al.* 1993). Clearly, more detailed calculations of the conditions for the appearance of wake structure, combined with detailed photometric modeling, would offer an efficient indirect method for inferring the actual elastic properties of particles in Saturn's rings.

An important result in the simulations of dense rings where collective wakes dominate is the strong increase of $c_x/r\Omega$ with radial distance a, proportional to a^3. According to simulations performed for $\tau = 0.4$ and $\Sigma = 480$ kg m^{-2}, $c_x/r\Omega$ reaches values on the order of 15 in the outer A-ring corresponding to $c_x \approx (r/1\text{ m})\ 0.2$ cm sec^{-1}. In the case of low τ, gravitational encounters yield $c_x/r\Omega \propto a^{1.5}$, reaching values of ≈ 6. This implies that even if ε is a constant close to zero, Saturn's A-ring should be far from the monolayer state which would be expected if self-gravity is omitted. For example, for $a = 130{,}000$ km an effective thickness of 15 m was obtained for identical 1-m particles. In the single size-distribution experiment described, for the same distance, $H \approx 65$ m for the submeter particles, and about 20 m for the largest particles. This increase in velocity dispersion is in accordance with the enhanced viscosity implied by the observations of the damping of density waves in Saturn's A-ring, especially the Mimas 5:3 bending wave at $a = 131{,}900$ km, for which the implied value for kinematic viscosity $\nu = 260$ cm^2 sec^{-1} (Shu *et al.* 1983). If we apply the approximate formula $\nu = c_x^2/2\Omega\ \tau/(1 + \tau^2)$ (Goldreich and Tremaine 1978) to the simulation for $a = 130{,}000$ km this yields $\nu \approx 40(r/1\text{ m})^2$ cm^2 sec^{-1}, which is on the same order if we assume that size distribution in Saturn's rings could be represented by a system with identical 2.5-m particles. However, it is unclear how well this formula applies to the present case with strong wakes where angular momentum is carried both by the "local" velocity dispersion and by the collective motions of the wakes. Another proposed explanation for increased velocity dispersion and viscosity is the input of kinetic energy from the numerous density waves in the outer A-ring (Lissauer *et al.* 1984). In fact, this also offers a possible explanation for the reduced asymmetry in the outermost A-ring, as discussed by Franklin *et al.* (1987) and Dones *et al.* (1993); if $Q_T \gg 2$ due to external energy input, the wake structure would again start to diminish, contrary to the trend that is seen in Fig. 14.

Although the simulation parameter values used referred to Saturn's rings the results can be extended to other planetary ring systems. For example, for the Uranian rings Eqs. (17) and (18) take the forms

$$\frac{c_{enc}}{r\Omega} = 9.3\left(\frac{a}{10^8\text{ m}}\right)^{1.5}\left(\frac{\rho}{900\text{ kg m}^{-3}}\right)^{0.5},$$

$$\frac{c_{wake}}{r\Omega} = 47Q_T\left(\frac{a}{10^8\text{ m}}\right)^{3}\left(\frac{\rho}{900\text{ kg m}^{-3}}\right)\tau.$$

Thus, assuming that $Q_T = 2$, $\rho = 900$ kg m^{-3}, $c_{wake}/r\Omega$ varies as $(7\text{–}12)\tau$ and $c_{enc}/r\Omega$ as 2.5–3.4 in the ring zone (42,000–51,000 km). These equations imply that self-grav-

itational forces should dominate over collisions in determining the equilibrium structure of dense ringlets. Indeed, according to French *et al.* (1991) and Esposito *et al.* (1991) Voyager radio occultation and multiwavelength observations indicate that the thickness of the ε ring is several tens of meters, while lower limits for the effective particle size and surface density are $r = 0.7$ m and $\Sigma = 800$ kg m^{-2}. For these minimum values, simulations suggest $H \approx 13$ m, consistent with the observationally deduced multilayer structure. However, the narrowness and eccentricity of the Uranian ringlets implies more complicated dynamical behavior than handled by the local simulations.

According to the present simulations (see also Salo 1992b), the formation of particle aggregates in the outer parts of Saturn's rings appears unavoidable if the individual particles have solid ice density and are not too elastic in their behavior. The properties of these groups were discussed here in terms of r_p, the sum of groups' and particles' physical radii relative to their combined Hill radii. According to Ohtsuki (1993), accretion is a typical outcome for an impact between a particle pair with $r_p < \frac{2}{3}$, whereas for larger r_p's the probability of accretion becomes increasingly smaller and vanishes for $r_p = 1$. In our simulations the r_p values for the outermost particles on the surfaces of the aggregates are in the range 0.7–0.9, so that at least temporary accretion is possible even if some of the group members spill over the group's Hill surface. However, the accretion condition $r_p < 1$, used for example by Longaretti (1989), is clearly too optimistic. Nevertheless, substantial clumpiness of the wake structure takes place for values corresponding to $r_p \approx 1$.

The subsequent evolution and the maximum size of the aggregates cannot be deduced from the present experiments, due to the limited number of particles in the simulations. Experiments with larger calculation regions, containing several such aggregates and allowing for their mutual interactions, would be needed. Also, in more realistic studies of accretion in the outer reaches of planetary rings it will be desirable to include a distribution of particles sizes. In principle, the new collisional method replacing impacts with a force model will facilitate the study of these problems.

ACKNOWLEDGMENTS

I thank Professor Alar Toomre and Dr. Luke Dones, for their most useful comments and suggestions for improvements.

REFERENCES

ARAKI, S. 1991. The dynamics of particle disks III. Dense and spinning particle disks. *Icarus* **90,** 139–171.

ARAKI, S., AND S. TREMAINE 1986. The dynamics of dense particle disks. *Icarus* **65,** 83–109.

BRIDGES, F. G., A. HATZES, AND D. N. C. LIN 1984. Structure, stability and evolution of Saturn's rings. *Nature* **309,** 333–335.

CANUP, R. M., AND L. W. ESPOSITO 1995. Accretion in the Roche Zone. I. Coexistence of rings and ringmoons. *Icarus* **113,** 331–352.

CUZZI, J. N., R. H. DURISEN, J. A. BURNS, AND P. HAMILL 1979. The vertical structure and thickness of Saturn's rings. *Icarus* **38,** 54–68.

DILLEY, J. P. 1993. Energy loss in collisions of icy spheres: Loss mechanism and size–mass dependence. *Icarus* **105,** 225–234.

DONES, L., J. N. CUZZI, AND M. R. SHOWALTER 1993. Voyager photometry of Saturn's A ring. *Icarus* **105,** 184–215.

DONES, L., AND C. PORCO 1989. Spiral density wakes in Saturn's A-ring? *Bull. Am. Astron. Soc.* **21,** 929. (abstract)

ESPOSITO, L. W., A. BRAHIC, J. A. BURNS, AND E. A. MAROUF 1991. Particle properties and processes in Uranus' rings. In *Uranus* (J. T. Bergstralh, E. D. Miner, and M. S. Matthews, Eds.), pp. 410–465. Univ. of Arizona Press, Tucson.

FRANKLIN, F. A., A. F. COOK II, R. T. F. BARRET, C. A. ROFF, G. E. HUNT, AND H. B. DE RUEDA 1987. Voyager observations of azimuthal brightness variations in Saturn's rings. *Icarus* **69,** 280–296.

FRENCH, R. G., P. D. NICHOLSON, C. C. PORCO, AND E. A. MAROUF 1991. Dynamics and structure of the Uranian rings. In *Uranus* (J. T. Bergstralh, E. D. Miner, and M. S. Matthews, Eds.) pp. 327–409. Univ. of Arizona Press, Tucson.

GOLDREICH, P., AND S. TREMAINE 1978. Velocity dispersion in Saturn's Rings. *Icarus* **34,** 227–239.

HÄMEEN-ANTTILA, K. A. 1984. Collisional theory of non-identical particles in a gravitational field. *Earth Moon Planets* **31,** 271–299.

HÄMEEN-ANTTILA, K. A., AND H. SALO 1993. Generalized theory of impacts in particulate systems. *Earth Moon Planets* **62,** 47–84.

HÄNNINEN, J., AND H. SALO 1994. Collisional simulations of satellite Lindblad resonances II: Formation of narrow ringlets. *Icarus* **108,** 325–346.

HATZES, A. P., F. G. BRIDGES, AND D. N. C. LIN 1988. Collisional properties of ice spheres at low impact velocities. *Mon. Not. R. Astron. Soc.* **231,** 1091–1115.

HILL, G. W. 1878. Researches in the lunar theory. *Am. J. Math.* **1,** 5–26.

HORNUNG, P., R. PELLAT, AND P. BARGE 1985. Thermal velocity equilibrium in the protoplanetary cloud. *Icarus* **64,** 295–307.

JULIAN, W. H., AND A. TOOMRE 1966. Non-axisymmetric responses of differentially rotating disks of stars. *Astrophys. J.* **146,** 810–827.

LISSAUER, J. J., F. H. SHU, AND J. N. CUZZI, 1984. Viscosity in Saturn's rings. In *Anneaux des Planetes* (A. Brahic, Ed.), IAU Colloq. Vol. 75, pp. 385–392. Cepadues Editions, Toulouse.

LONGARETTI, P-Y. 1989. Saturn's main ring particle size distribution: An analytical approach. *Icarus* **81,** 51–73.

LUKKARI, J., AND H. SALO 1984. Numerical simulations of collisions in self-gravitating systems. *Earth Moon Planets* **31,** 1–13.

OHTSUKI, K. 1992. Equilibrium velocities in planetary rings with low optical depth. *Icarus* **95,** 265–282.

OHTSUKI, K. 1993. Capture probability of colliding planetesimals: Dynamical constraints on accretion of planets, satellites, and ring particles. *Icarus* **106,** 228–246.

RICHARDSON, D. C. 1993. A new tree code method for simulation of planetesimal dynamics. *Mon. Not. R. Astron. Soc.* **261,** 396–414.

SALO, H. 1987a. Collisional evolution of rotating, non-identical particles. *Earth Moon Planets* **38,** 149–181.

SALO, H. 1987b. Numerical simulations of collisions between rotating particles. *Icarus* **70,** 37–51.

SALO, H. 1991. Numerical simulations of dense collisional systems. *Icarus* **90,** 254–270. See also Erratum, *Icarus* **92,** 367–368.

SALO, H. 1992a. Numerical simulations of dense collisional systems. II. Extended distribution of particle sizes. *Icarus* **96,** 85–106.

SALO, H. 1992b. Gravitational wakes in Saturn's rings. *Nature* **359,** 619–621.

SALO, H., AND J. LUKKARI 1982. Self-gravitation in Saturn's rings. *Moon Planets* **27,** 5–12.

SALO, H., J. LUKKARI, AND J. HÄNNINEN 1988. Velocity dependent coefficient of restitution and the evolution of collisional systems. *Earth Moon Planets* **43,** 33–43.

SHU, F. H. 1984. Waves in planetary rings. In *Planetary Rings* (R. Greenberg and A. Brahic, Eds.), pp. 513–561. Univ. of Arizona Press, Tucson.

SHU, F. H., J. N. CUZZI, AND J. J. LISSAUER 1983. Bending waves in Saturn's rings. *Icarus* **53,** 185–206.

STEWART, G. R., D. N. C. LIN, AND P. BODENHEIMER 1984. Collision induced transport properties in planetary rings. In *Planetary Rings* (R. Greenberg and A. Brahic, Eds.), pp. 447–512. Univ. of Arizona Press, Tucson.

STEWART, G. R., AND G. W. WETHERILL 1988. Evolution of planetesimal velocities. *Icarus* **74,** 542–553.

TOOMRE, A. 1964. On the gravitational stability of a disk of stars. *Astrophys. J.* **139,** 1217–1238.

TOOMRE, A. 1990. Gas-hungry Sc spirals. In *Dynamics and Interactions of Galaxies* (R. Wielen, Ed.), pp. 292–303. Springer, Berlin.

TOOMRE, A., AND A. J. KALNAJS 1991. Spiral chaos in an orbiting patch. In *Dynamics of Disc Galaxies* (B. Sundelius, Ed.), pp. 341–358. Göteborg, Sweden.

WEIDENSCHILLING, S. J., C. R. CHAPMAN, D. DAVIS, AND R. GREENBERG 1984. Ring particles: Collisional interactions and physical nature. In *Planetary Rings* (R. Greenberg and A. Brahic, Eds.), pp. 367–415. Univ. of Arizona Press, Tucson.

WISDOM, J., AND S. TREMAINE 1988. Local simulations of planetary rings. *Astron. J.* **95,** 925–940.